Oxygen metabolism-balanced engineered hydrogel microspheres promote the regeneration of the nucleus pulposus by inhibiting acid-sensitive complexes

Ziang Li [a,1], Feng Cai [a,1], Jincheng Tang [a,1], Yichang Xu [a,1], Kaijin Guo [b], Zonghan Xu [a], Yu Feng [a], Kun Xi [a,*], Yong Gu [a,**], Liang Chen [a,***]

[a] Department of Orthopedics, the First Affiliated Hospital of Soochow University, Orthopedic Institute, Soochow University, 188 Shizi Road, Suzhou, Jiangsu, 215006, PR China
[b] Department of Orthopedics, the Affiliated Hospital of Xuzhou Medical University, 99 Huaihai West Road, Xuzhou, Jiangsu, 221000, PR China

ARTICLE INFO

ABSTRACT

Intervertebral disc degeneration (IVDD) is commonly caused by imbalanced oxygen metabolism-triggered inflammation. Overcoming the shortcomings of antioxidants in IVDD treatment, including instability and the lack of targeting, remains challenging. Microfluidic and surface modification technologies were combined to graft chitosan nanoparticles encapsulated with strong reductive black phosphorus quantum dots (BPQDs) onto GelMA microspheres via amide bonds to construct oxygen metabolism-balanced engineered hydrogel microspheres (GM@CS-BP), which attenuate extracellular acidosis in nucleus pulposus (NP), block the inflammatory cascade, reduce matrix metalloproteinase expression (MMP), and remodel the extracellular matrix (ECM) in intervertebral discs (IVDs). The GM@CS-BP microspheres reduce H_2O_2 intensity by 229%. Chemical grafting and electrostatic attraction increase the encapsulation rate of BPQDs by 167% and maintain stable release for 21 days, demonstrating the antioxidant properties and sustained modulation of the BPQDs. After the GM@CS-BP treatment, western blotting revealed decreased acid-sensitive ion channel-3 and inflammatory factors. Histological staining in an 8-week IVDD model confirmed the regeneration of NP. GM@CS-BP microspheres therefore maintain a balance between ECM synthesis and degradation by regulating the positive feedback between imbalanced oxygen metabolism in IVDs and inflammation. This study provides an in-depth interpretation of the mechanisms underlying the antioxidation of BPQDs and a new approach for IVDD treatment.

1. Introduction

Reactive oxygen species (ROS), which include superoxide anions (O^{2-}), hydroxyl radicals (OH^-), and hydrogen peroxide (H_2O_2), are metabolic byproducts in the respiratory chain of the inner mitochondrial membrane and play critical roles in cell signaling and homeostasis *in vivo* [1]. The imbalance between ROS generation and scavenging is the primary cause of oxidative stress-induced injury. In tissue injury, cellular mitochondrial respiratory chain transmission is impaired, and large amounts of ROS are generated to overflow into the endogenous scavenging system. Imbalanced oxygen metabolism leads to the accumulation of succinate and enhances lipid peroxidation in tissues, which downregulates proteoglycan synthesis and triggers the degradation of the extracellular matrix (ECM) [2]. In addition, ROS act as second messengers in concert with Ca^{2+} enriched in mitochondria to stimulate the opening of the mitochondrial permeability transition pore, leading

to the release of a large number of apoptotic factors, such as Cytc, AIF, and SMAC, and inducing apoptosis [3]. This impairs mitochondrial function and activates the nuclear factor kappa B (NF-κB), mitogen-activated protein kinase (MAPK), and other inflammatory signaling pathways to secrete inflammatory factors such as interleukin (IL)-1β and tumor necrosis factor (TNF)-α, thereby inducing the inflammatory cascade and various secondary diseases [4,5]. Intervertebral discs (IVDs) in the human body are surrounded by upper and lower endplates and anterior and posterior longitudinal ligaments, which form a confined hypoxic-ischemic microenvironment with the accumulation of lactic acid and ROS. This constitutes the structural basis of intervertebral disc degeneration (IVDD) [6]. A previous study revealed that hydrogen peroxide (H_2O_2) can enhance the concentration of lactic acid and the expression of proton-gated acid-sensitive ion channel-3 (ASIC-3) in NS20Y cells and primary cultured mouse cortical neurons [7]. Zhao et al. demonstrated that ASIC-3 is involved in the activation of nucleus pulposus (NP) inflammatory signals and triggers an inflammatory response, which leads to the enhanced expression of matrix metalloproteinase (MMP) and degradation of type II collagen (COL-II), thereby accelerating IVDD [8]. However, it is unclear whether excessive ROS in the IVDD microenvironment can cause an increase in ASIC-3 expression of NP and form a vicious positive feedback circle.

In recent years, precision medicine has promoted the rapid development of targeted therapies. Local injections in IVDs have been used to neutralize ROS and block the positive feedback of the ROS chain [9]. However, common antioxidant drugs, such as melanin, are not conducive to binding to biological scaffolds due to their deformability in organic solvents [10]. N-acetylcysteine (NAC) has a short half-life, and low concentrations of reductive substances remain in target organs despite multiple administrations [11,12]. These shortcomings limit the clinical applications of these drugs. Therefore, the development of a stable and efficient ROS neutralization method to inhibit the pathophysiological development of injured tissues is urgently needed.

Recently, the application of nanomaterials has paved the way for the in-depth study of pathophysiological development, remodeling, and regeneration [13–16]. Black phosphorus (BP), for example, is a phosphorus allotrope with a wide and promising application in the biomedical field and is an analog of two-dimensional semiconductor nanostructures [17–19]. The preparatory process of BP is relatively stable, and it degrades into non-toxic phosphate ions *in vivo*, which ensures biological safety [20,21]. Inspired by the strong reductive property of BP, Hou et al. applied a BP nanosheet as a ROS scavenger to mitigate ROS-triggered acute kidney injury and demonstrated its remarkable antioxidant capacity, which is superior to that of the conventional antioxidant NAC [22]. In addition, black phosphorus quantum dots (BPQDs) have a larger surface area compared to nanosheets and can scavenge excess ROS from degenerated discs more efficiently [23]. Therefore, the application of BPQDs may provide a new therapeutic platform for IVDD. However, the strong reducibility and smaller nanoparticle sizes of BPQDs make them susceptible to oxidation and hinder their long-term effects in regulating the oxygen metabolism balance in IVDs [24]. Currently, liposomal and polymeric nanoparticles have facilitated the maintenance of the bioactivity of the loadings and prolonged the duration of their biological effects, but there remain various drawbacks that limit their use for IVDD treatment. For example, liposomes exhibit poor sustained release [25], and poly (lactic-co-glycolic acid) (PLGA) has shown a slow degradation rate [26]. Chitosan nanoparticles (CS) are a suitable material for BP protection due to their simple preparation, good biocompatibility, and large number of positively charged functional amino groups on their surfaces that can effectively bind to negatively charged BPQDs [27–29]. Therefore, using CS as BPQD carriers may improve reducibility and encapsulation rates, which would allow the BPQDs to maintain the oxygen metabolic balance in IVDD.

IVDs are load-bearing tissue structures that connect the vertebral bodies of the spine. They are pivotal in transmitting ergonomic stress

and are in a long-term, high-pressure state. Direct local injections of nanoparticles may result in needle track leakage, diffusion, and a lack of mechanical stress to maintain disc height [30,31]. Therefore, the nanoparticles that are currently in use rely on transport carriers to improve their injection efficiency and targeting. Organometallic frameworks and hydrogels are currently used as transport carriers for IVDD treatment; however, there are still significant drawbacks [32,33]. For example, compression tends to lead to the collapse of the overall structure of large hydrogels and causes subsequent complications [34]. Organic molecules, such as PLGA, is prone to forming acidic byproducts after degradation, which further deteriorates the microenvironment of IVDs and leads to inflammation [35,36]. Therefore, an injectable biomaterial with the appropriate mechanical strength and uniform loading ability of nanoparticles is required to achieve long-term ROS neutralization by BPQDs. Gelatin methacrylate anhydride (GelMA) has exhibited excellent biocompatibility and can be fabricated precisely into uniform hydrogel microspheres using microfluidic technology. Its porous surface formed after freeze-drying can further graft nanoparticles. GelMA hydrogels have therefore become a topic of interest for the injectable therapies of IVDD [37,38].

Based on the ROS-induced pathological changes in IVDD, we prepared oxygen metabolism-balanced engineered injectable hydrogel microspheres (GM@CS-BP) by grafting CS loaded with BPQDs onto the surfaces of GelMA porous microspheres via amide bonds. The GM@CS-BP composite microspheres achieved the efficient and uniform loading of nanoparticles and were capable of targeted implantation into the IVDs microenvironment through a micro syringe [39]. This allowed for the sustained release of the strong reductive BPQDs from CS, neutralized ROS in situ, alleviated oxidative stress-induced injury, and improved the oxygen metabolism microenvironment in the IVDs. GM@CS-BP inhibited apoptosis, ameliorated extracellular acidosis, downregulated the expression of acid-sensing complexes, and blocked the inflammatory cascade triggered by the activation of downstream inflammatory pathways. In the rat IVDD model, the GM@CS-BP microspheres provided mechanical stress, reduced MMP expression, promoted NP regeneration, and remodeled the structure and function of the ECMs of the degenerated IVDs. The oxygen metabolism-balanced engineered hydrogel microspheres may provide a new theoretical basis for the use of BP as a reductive agent to delay IVDD. The microspheres further highlight the regenerative application of biomaterials in the local acidic microenvironment under oxidative stress (Scheme 1).

2. Results and discussion

2.1. The relationship between oxidative stress, acid-sensitive complexes, and IVDs

Acid-sensitive ion channels (ASICs) are a subfamily of proton-gated channels and are susceptible to activation by extracellular acidosis, lactate, and arachidonic acid [6]. The levels of ASIC-1, -2, and -3 were significantly increased in degenerated NP cells, with ASIC-3 being predominant. It has been found that ASIC-1a may increase MMP activity through the NF-κB signaling pathway in endplate chondrocytes. At high extracellular lactate concentrations, ASIC-3 expression is upregulated in NP cells, and NLRP3 inflammatory vesicles are activated, leading to the release of IL-1β, which is an important inflammatory factor in IVDD. This activates the inflammatory cascade [40]. As the interaction between acid-sensitive complexes and ROS has rarely been reported, we explored the possible positive feedback cycle between ROS and ASIC-3 in the NP. First, the NP cells were stimulated with different concentrations of H_2O_2 (Fig. 1A). We then used a lactate detection kit [41] and found that, although no significant difference existed between the 50-μM H_2O_2 simulation and control groups, the lactate concentration increased by 1.83-fold under 400-μM H_2O_2 stimulation compared to the control group (Fig. 1B). ROS can therefore induce the accumulation of extracellular lactic acid and an extracellular acidotic environment. The
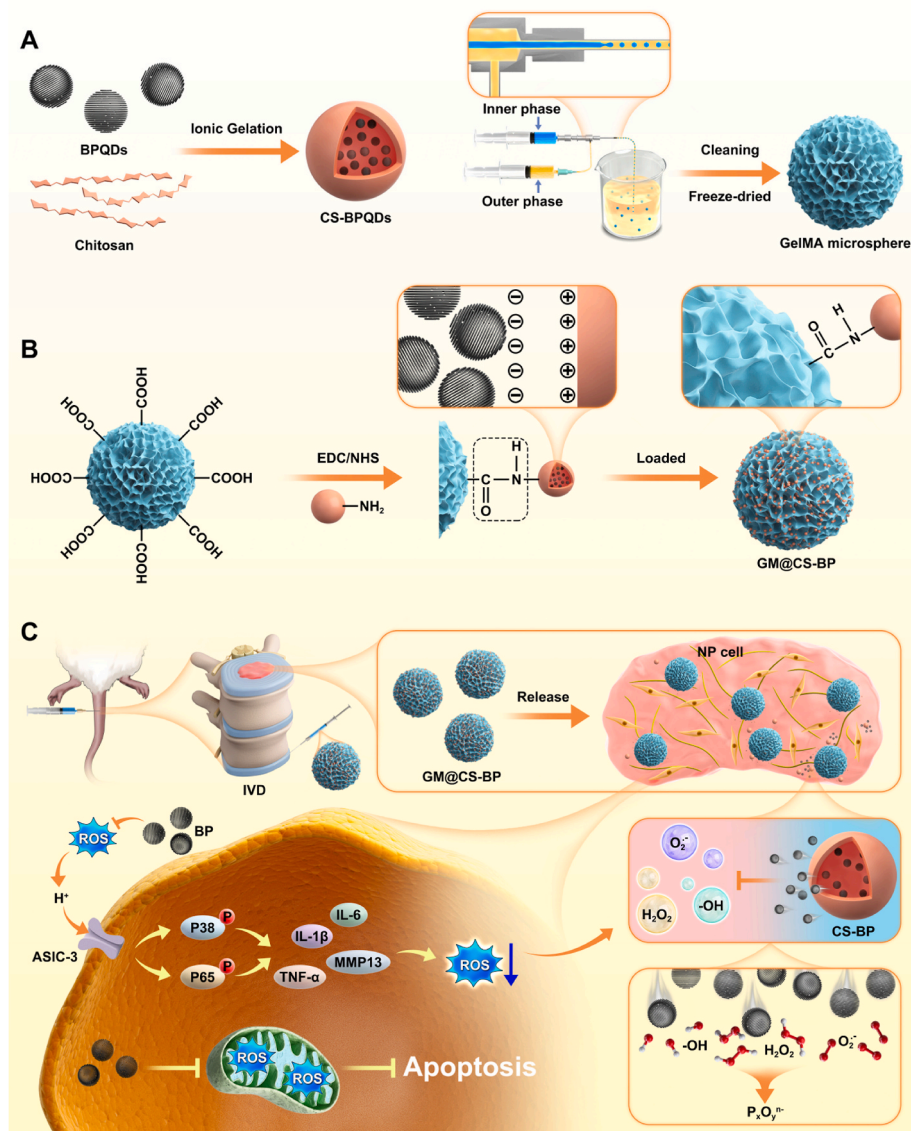
Scheme 1. Schematic illustration. A) Preparation of BPQDs, CS nanoparticles, and GelMA microspheres. B) Activation and grafting of GelMA and CS-BP nano-particles. C) Targeted injection of the oxygen metabolism-balanced engineered hydrogel microspheres in rat IVDs and the underlying therapeutic mechanisms.

ASIC-3 protein content was detected by western blotting (Fig. 1C), and its expression was correlated with the concentration of H_2O_2 stimulation (Fig. 1L). Under 400-μM H_2O_2 stimulation, the pH value reached 6.53 ± 0.12, which was significantly lower than that of the control group (Fig. 1D). Immunofluorescent staining of ASIC-3 was subsequently performed (Fig. 1E), and it was found that H_2O_2 stimulation enhanced ASIC-3 fluorescence intensity in NP cells. The semiquantitative results showed a 5.8-fold increase in ASIC-3 fluorescence intensity compared to the control group (Fig. 1M). An IVDD model was successfully constructed by caudal punctures in rats [42], and digital radiography (DR) was performed 4 weeks later (Fig. 1F). A significant difference in disc height was found between the blank and negative control (NC) groups punctured alone ($p < 0.01$, Fig. 1N, Table S1 Supporting Information). Magnetic resonance imaging (MRI) were also performed (Fig. 1G), and MRI grading was evaluated according to the Thomson classification [38]. The MRI grading in the NC group was higher than that in the control group (Fig. 1O). Hematoxylin-eosin (H&E) staining and Safranin O/Fast green staining (Fig. 1H and I) showed significant atrophy in the NP in the NC group, with indistinguishable borders and a massive dissipation of proteoglycans, indicating increased IVDD (Fig. 1P). The

expression of ROS and ASIC-3 in the degenerated discs was further assessed. Heme oxygenase (HO-1) is a major regulatory enzyme involved in the intracellular defense against oxidative stress and anti-inflammatory, antioxidant, and apoptotic processes [43]. When subjected to multiple stimuli, especially oxidative stress, HO-1 expression is upregulated, indicating that high HO-1 expression demonstrates ROS stimulation in tissues. *In vivo* staining (Fig. 1J) showed a substantial increase in HO-1 fluorescence intensity in the NC group compared to that in the control group (Fig. 1Q), while ASIC-3 immunohistochemistry (Fig. 1K) revealed a 4.6-fold increase in its expression in the NC group compared to that in the control group ($p < 0.001$, Fig. 1R). This indicated the presence of oxidative stress and ASIC-3 in the IVDD model. These results show that ROS may induce downstream inflammation through the upregulation of acid-sensitive complex expression in NP cells and provide new insights into potential anti-ROS therapies for IVDD.

2.2. Preparation and characterization of BPQDs and CS-BP

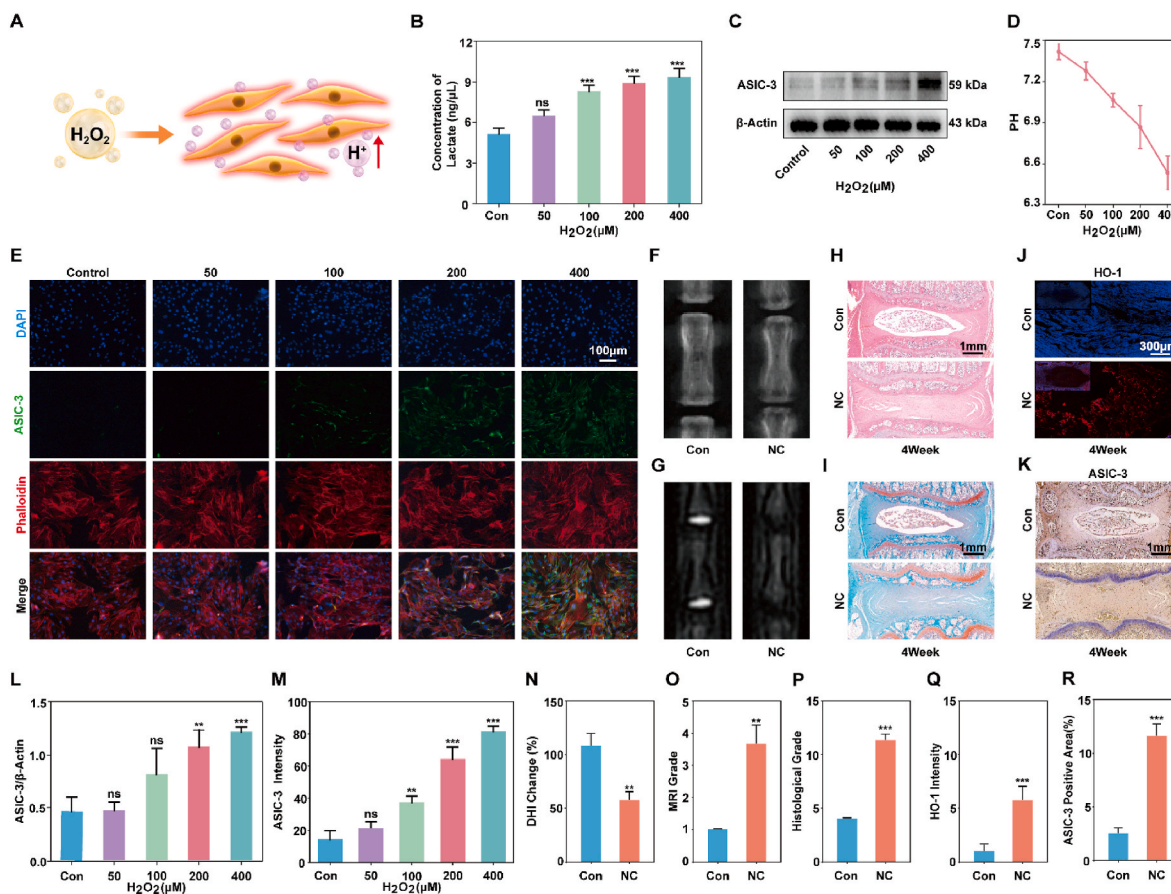BPQDs are easily oxidized in air, and their small particle size

Fig. 1. The relationship between H₂O₂, acid-sensitive complexes, and IVDD. A) Schematic diagram of extracellular acidosis in the NP induced by H_2O_2 stimulation. B–E) The extracellular lactic acid content, Western blot of the ASIC-3 protein, pH value, and immunofluorescent staining of ASIC-3 in NP cells after stimulation with different concentrations of H_2O_2. F–K) DR photos, MR scan, H&E staining, Safranin O/Fast green staining, HO-1 immunofluorescence, and ASIC-3 immunohistochemistry after 4 weeks in a rat caudal IVDD model. L) Semiquantitative analysis of ASIC-3 protein expression. M) ASIC-3 immunofluorescent intensity. N–R) DHI, MRI grading, histological grading, semiquantitative analysis of the HO-1 intensity, and semiquantitative analysis of ASIC-3 histochemistry after 4 weeks (n = 3; all data are presented as the mean ± standard deviation; *p < 0.05; **p < 0.01; ***p < 0.001; the comparison of the groups with different H_2O_2 concentrations and the blank control group was performed using a one-way ANOVA and Tukey's test, respectively; ns, not significant).

determines their instability during preparation [18]. CS were selected as protective agent for BPQDs due to their excellent biocompatibility and the abundant amino groups on their surface. BPQDs were first prepared via liquid-phase exfoliation, as described in a previous study (Fig. 2A) [44,45]. As observed before and after high-intensity sonication (Fig. 2B), the simple BP nanosheets were dark black in air and turned light yellow after constant centrifugation and sonication. The CS-BP was prepared using an ionic cross-linking method. Chitosan molecules have abundant NH3 groups that can react with the negatively charged phosphoric ions of sodium tripolyphosphate (TPP) to form cross-linked CS. During the process of cross-linking and hardening, BPQDs were adsorbed, which may help sustain their encapsulation efficiency [46, 47]. BPQDs and CS-BP were observed using transmission electron microscopy (TEM) (Fig. 2C). The BPQDs generally presented as circular structures of different sizes, whereas in the CS-BP composite structure, the BPQDs were uniformly distributed in and around the CS (Fig. 2D) [48]. To verify the successful connection between the CS and BPQDs, Raman scattering spectroscopy was used on CS-BP (Fig. 2E). In the Raman spectrum, the representative peaks of simple BPQDs were A_g^1:358.4, B_{2g}^2:438.2, and A_g^2:467.1 cm^{-1}, and the representative peaks of BP were detected in the CS-BP nanoparticles [49,50]. The sizes of the BPQDs and CS were further analyzed (Fig. 2F and G, and S1). The diameters of the BPQDs were distributed at 4.8 ± 2.2 nm, and CS and CS-BP particles showed a general distribution of 78.56 ± 21.45 nm, which was consistent with the morphological results of the TEM

analysis. The Zeta potential of the nanoparticles was detected (Fig. 2H), and the BPQDs exhibited a Zeta potential of −19.63 ± 2.86 mV due to the phosphate anion formed by oxidation on their surface, while the CS showed a Zeta potential of 34.43 ± 3.82 mV because of their abundant amino groups. The Zeta potential of CS-BP formed by ionic cross-linking was 19.37 ± 2.46 mV, which was significantly lower than that of CS. The CS were therefore successfully bonded to the BPQDs.

2.3. Preparation and characterization of GM and GM@CS-BP microspheres

GelMA microspheres are ideal carriers for reductive agents in injectable therapies due to their excellent biocompatibility and abundant surface pores [51]. However, simple physical absorption may lead to problems such as the uneven distribution or instability of the loaded drug in the environment [13]. Therefore, nanoparticle grafting through amide bonding was chosen in this study to improve the stable loading capacity of hydrogel microspheres for nanoparticles to adapt to the high-pressure environment of IVDD. Using the microfluidic technology available in our research group, GelMA microspheres were prepared by co-flow shearing formed by the continuous and dispersed phases of the coaxial electrospinning nozzle (Fig. 3C) [52]. Through simple physical adsorption, GM and BP were combined to construct the GM-BP group, which was compared with the GM@CS-BP group in subsequent experiments to verify the ability of CS to improve the encapsulation and
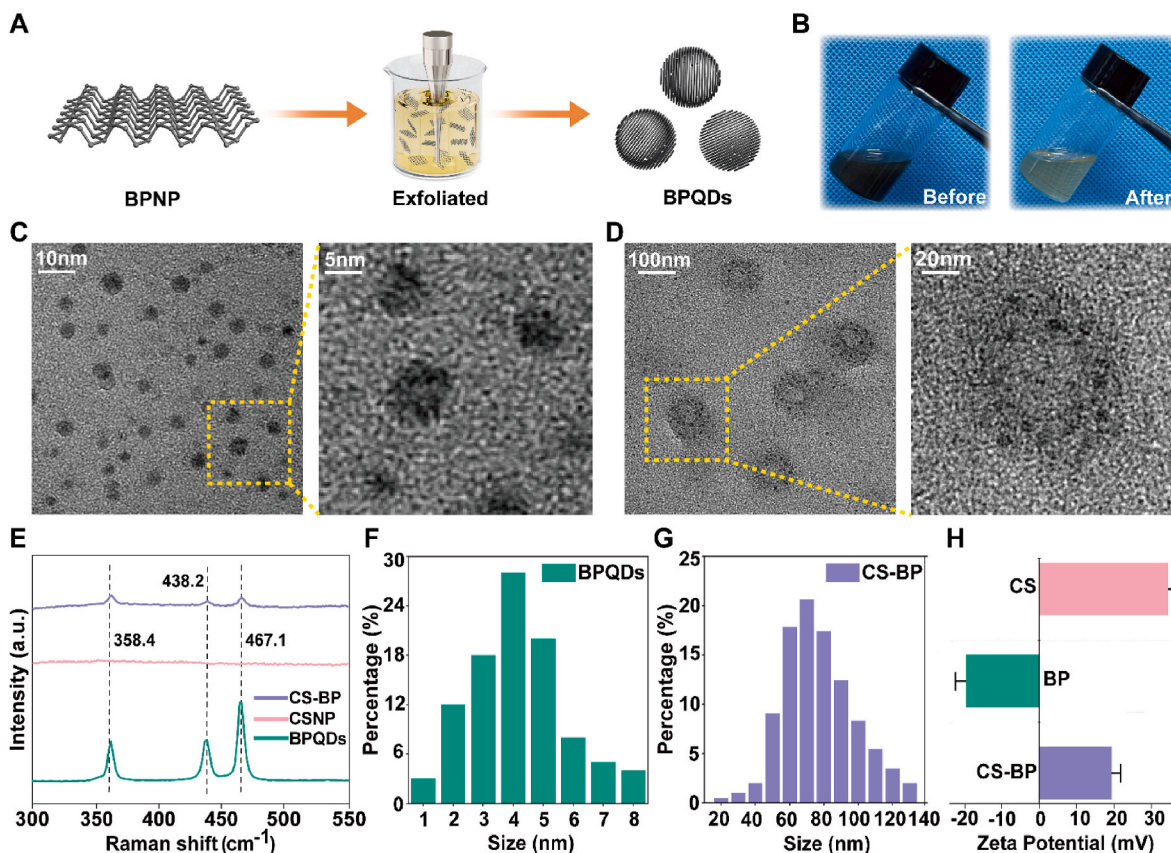
Fig. 2. Preparation and characterization of BPQDs and CS. A) Schematic diagram of BPQDs prepared by liquid-phase exfoliation. B) BPQDs before and after sonication. C) Morphology of BPQDs under TEM. D) Morphology of CS-BP under TEM. E) Raman spectra of BPQDs, CS, and CS-BP. F) Particle sizes of the BPQDs. G) Particle size of CS-BP. H) Zeta potential.

sustained release of the BPQDs. The amino group in CS was reacted with the carboxyl group of the microspheres under the 1-ethyl-3-[3-dimethy-laminopropyl] carbodiimide hydrochlorid e (EDC)/N-hydrox-ysuccinimide (NHS) system (Fig. 3A, **B**) to complete the nanoparticle grafting [39]. The GM@CS-BP microspheres possessed relatively uniform surface pores with a distribution of 5.6 ± 4.05 μm (Fig. 3K), which enabled the GM microspheres to fully combine with the CS-BP nanoparticles and provided the morphological basis for the effective drug-loading of the GM microspheres (Fig. 3D). The size distribution of the microspheres was 68.7 ± 21.25 μm (Fig. 3L), which did not change significantly between the simple GM and GM-BP microspheres (Fig. S2). The local magnification of the pores on the microsphere surfaces showed the presence of uniformly dense CS-BP nanoparticles (marked by red arrows), which proved the connection and effective loading. The successful injection of the microspheres through a needle syringe provided the basis for the planned IVDD treatment. A micro syringe with a small needle tip was therefore chosen to simulate the injection apparatus for rat IVDD. The microspheres were successfully injected with uniform dispersion while maintaining their intact morphology (Fig. 3F). The GelMA microspheres were uniformly arranged in the oil phase and did not exhibit significant changes in size and structure for 30 min (Fig. 3G). Infrared spectroscopy (FT-IR) and energy dispersive spectroscopy (EDS) analyses were performed to verify the binding between the GM microspheres and CS. As shown in the FT-IR spectra (Fig. 3H), specific chemical groups of both GelMA and CS were observed in the GM@CS-BP spectra, indicating that GelMA and CS formed a good mixture [53]. Compared to the GelMA microspheres alone, GM@CS-BP showed a significant downward shift at the 3300 cm^{-1} peak, indicating the presence of –OH, whereas the decrease in the peak at 1640 cm^{-1} represented the presence of C═C vibrations. The comparison with the IR spectrum of

CS revealed a decrease in the peak at both 1620 and 1530 cm^{-1}, which may have been related to the NH3 on CS [54]. There were no significant changes in the GM@CS-BP and GM@CS groups. The elemental contents of GM and GM@CS-BP were compared using EDS (Fig. 3I). As expected, the phosphorus (P) element in GM@CS-BP was substantially elevated by 10.2% compared to that in the GM group. This indicated the successful grafting of the CS on the microsphere surfaces and the presence of released BPQDs. A small amount of nitrogen (N) was also detected on the surfaces of the GelMA microspheres as some of the amino groups had not been completely replaced in the preparation of the GelMA [55]. In summary, the successful grafting of GelMA microspheres and CS-BP nanoparticles was demonstrated by FT-IR and EDS.

The ability of GM@CS-BP to release BPQDs is also crucial for treating IVDD. Partial BP nanosheets were likely to be oxidized to P–O–P and terminated with o'-P2O5 or phosphoric acid. These functional groups can stabilize the BP nanosheets for biomedical applications. As BP is not a conventional drug, plotting its release profile is challenging. To verify the consistent and effective release of BP, P was measured in solution using inductively coupled plasma optical emission spectrometry (ICP) [56]. The encapsulation efficiency was calculated using Equation (1). Owing to the simple preparation process, the CS-BP group exhibited the highest encapsulation efficiency (the average encapsulation rate was 67.83%). The average encapsulation rate of GM@CS-BP to BP (60.63%) was much higher than that obtained using physical adsorption (the average encapsulation rate of GM-BP was 36.31%), which confirmed a 1.67-fold increase in the encapsulation rate (Fig. 3J). To delineate the release curve of the BPQDs, the supernatants of the microspheres at specified timepoints were detected, and the cumulative release of P was calculated to represent the BP release pattern. The release profiles of the microspheres and BP by physical adsorption exhibited a rapid abrupt
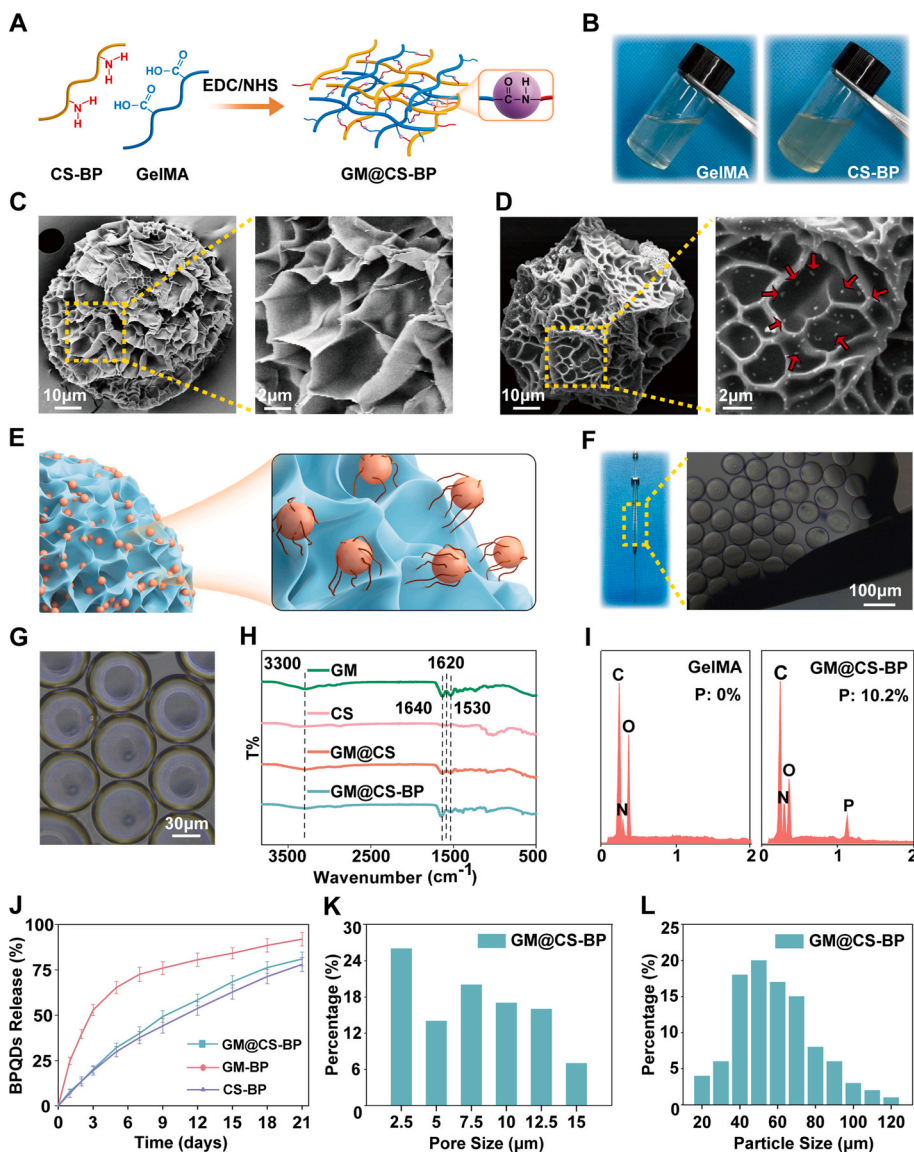
Fig. 3. Preparation and characterization of GelMA microspheres and GM@CS-BP. A) Schematic diagram of the grafting of CS-BP and GelMA. B) GelMA and CS-BP. C) Morphology of GelMA microspheres under SEM. D) Morphology of GM@CS-BP microspheres under SEM. E) Local magnification of GM@CS-BP. F) GM@CS-BP microspheres injected through the micro syringe. G) Morphology of oil-phased GM@CS-BP under a light microscope. H) FT-IR analysis. I) EDS analysis. J) Cumulative release curve of BPQDs detected by ICP. K) Pore sizes of the GM@CS-BP microspheres. L) Particle sizes of the GM@CS-BP microspheres.

release within five days. In contrast, although the release of BP after encapsulation by CS was lower within five days, a more regular and continuous release was maintained in the latter process. The GM@CS-BP and CS-BP groups showed decent release ability in both the early and late stages. This may be because CS protected BP from oxidative loss during preparation, whereas the break of the electrostatic force formed by the CS and BPQDs was able to release BPQDs continuously and efficiently. These results demonstrate the encapsulation and sustained release capabilities of the oxygen metabolic-balance functionalized hydrogel microspheres.

2.4. The anti-apoptotic and antioxidant capacities and biocompatibility of GM@CS-BP

Given the long-term ischemic and hypoxic microenvironment of IVDs, the dynamic balance between the generation and scavenging of ROS is disrupted, triggering the accumulation of a large number of ROS products inside IVDs [12]. The accumulation of ROS products causes an increase in the level of tissue lipid peroxidation, triggering changes in the mitochondrial membrane potential, an increase in the permeability of the outer mitochondrial membrane, and a large outflow of apoptotic factors that eventually lead to apoptosis [3]. In addition, ROS product

accumulation activates downstream inflammatory pathways, leading to the release of large amounts of inflammatory factors inside IVDs. The most representative H_2O_2 in ROS was therefore chosen to simulate the oxidative stress environment inside IVDs, and the required H_2O_2 concentration was verified using the Cell Counting Kit (CCK)-8 assay. As shown in Fig. 4B, when stimulated with 50 μM of H_2O_2, NP cell activity was not significantly inhibited, whereas when stimulated with 200 μM of H_2O_2, NP cell growth was significantly inhibited compared to the control group, with its activity being nearly half that of the control group. In contrast, H_2O_2 stimulation at 400 μM resulted in cell death in more than half of the NP cells. Based on previous studies, an H_2O_2 concentration of 200 μM was screened as an intervention condition to simulate the oxidative stress environment in IVDs [57]. In this study, the anti-ROS ability of GM@CS-BP was a key factor for assessment, and the DCFH-DA probe was chosen to verify the H_2O_2 scavenging ability of the material [58] and validate its appropriate ratio. In brief, CS-BP solutions and GM microspheres of different volume ratios (1:1, 1:2, 1:4, 1:8, and 1:16) were chemically linked through amide bonds, and the composite microspheres were co-cultured with NP cells. The co-culture system was stimulated with H_2O_2 for 6 h, after which a DCFH-DA fluorescent probe was used to detect ROS levels. Intra-environmental ROS fluorescence intensity was significantly reduced when the volume ratio of the CS-BP
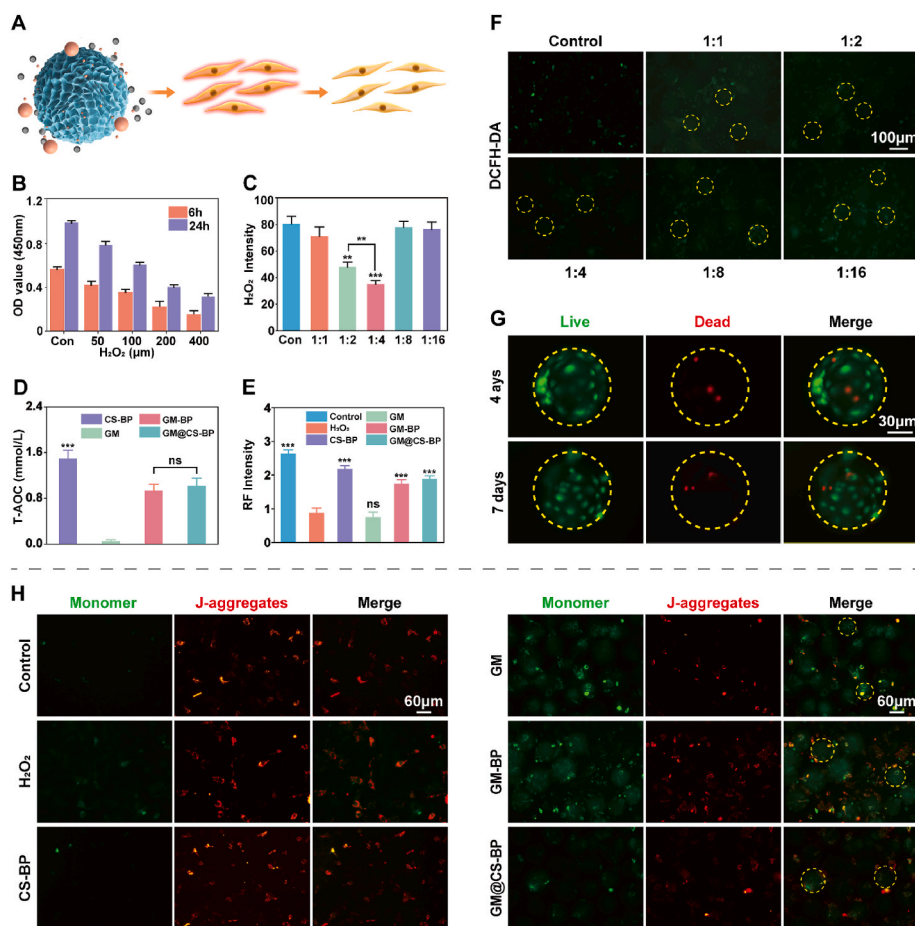
Fig. 4. The biocompatibility and antioxidant and anti-apoptotic capacities of GM@CS-BP. A) Schematic diagram of GM@CS-BP against oxidative stress in NP cells. B) CCK-8 assay of NP cells after stimulation with different concentrations of H_2O_2 for 6 and 24 h. C) Semiquantitative analysis of the anti-ROS ability of materials at different GM-to–CS–BP ratios detected by a DCFH-DA fluorescent probe. D) Total antioxidant capacities of CS-BP, GM, GM-BP, and GM@CS-BP. E) Semiquantitative analysis of the relative fluorescence intensity of JC-1 mitochondrial membrane potential in a co-culture of materials and cells after H_2O_2 stimulation. F) DCFH-DA fluorescent probe to detect intracellular ROS. G) Live/dead staining of microspheres and cells co-cultured after 4 and 7 days. H) Detection of JC-1 mitochondrial membrane potential in the co-culture of materials and cells after H_2O_2 stimulation. Yellow circles represent different microspheres. (n = 3; all data are presented as the mean ± standard deviation and were compared by a one-way ANOVA and Tukey's test; *p < 0.05; **p < 0.01; ***p < 0.001; ns, not significant).

nanoparticle solution to GM microsphere solution was 1:2 (**p < 0.01, compared to the control and volume ratio 1:8 and 1:16 groups) and 1:4 (***p < 0.001, compared to the control and volume ratio 1:8 and 1:16 groups) (Fig. 4F). The lowest H_2O_2 intensity was detected at a volume ratio of 1:4 (**p < 0.01, compared with the volume ratio 1:2 group), indicating that the anti-ROS ability of the material had reached its highest peak (Fig. 4C) with a 2.29-fold decrease in fluorescence intensity compared with the control group. Additionally, increasing or decreasing the volume ratio reduced the anti-ROS ability of the material. The reason for this may have been the lack of an antioxidative capacity of the material at a low BPQD content, while the composite microspheres may have over-reduced O_2 when the BPQDs were excessive, thereby resulting in an unimproved hypoxic environment. The total antioxidant capacity (T-AOC) of CS-BP, GM, GM-BP, and GM@CS-BP was also detected 6 h after preparation [59] and was presented as the Trolox-equivalent antioxidant capacity (Fig. 4D). Notably, CS-BP showed strong antioxidant capacity. This is due to the fact that CS-BP can directly and effectively release BPQDs. The GM microspheres exhibited almost no antioxidant capacity, whereas the antioxidant capacity of GM-BP and GM@CS-BP substantially increased. The 6 h T-AOC results indicated that GM-BP had a considerable antioxidant capacity due to the rapid abrupt release of GM-BP. As shown in the fluorescence semiquantitative results of the DCFH-DA probe, the materials possessed a satisfactory ROS scavenging ability, and the proper volume ratios of the GM microspheres and CS-BP nanoparticle solution were screened, which established the basis for subsequent experiments.

A live/dead cell assay was then performed (Fig. 4G, **S3**). At first, the cells were evenly distributed on the microspheres. On day 7, an increase in live cells on the microspheres was observed, while the increase in dead cells was not significant. This indicated that the composite

microsphere scaffold may be a suitable biological scaffold for the growth of NP cells. The mitochondria are the main sites of ROS production. ROS induce a decrease in mitochondrial transmembrane potential at the site of the mitochondrial respiratory chain complex, allowing apoptosis-related proteins to translocate across the membrane into the cytoplasm and trigger apoptosis. Membrane potential was verified using the JC-1 kit. The JC-1 probe was present in mitochondria as polymers (J-aggregates) and exhibited a red color under a fluorescence microscope at a high mitochondrial membrane potential, while its monomer exhibited green fluorescence at a low mitochondrial membrane potential (Fig. 4H) [60]. Without intervention with H_2O_2 as the control, CS-BP, GM, GM-BP, and GM@CS-BP were compared by co-culturing the microspheres and cells after H_2O_2 treatment (Fig. 4E). The CS-BP group showed strong anti-apoptotic ability owing to the biological effects triggered by the release of reductive BPQDs. The H_2O_2 and GM groups mainly showed green fluorescence, with no significant difference in their relative fluorescence intensity (RFI; RFI = J-aggregates/monomer) compared with the control group. This indicated a low mitochondrial membrane potential in the H_2O_2 and GM groups, and that the cells were in the early stages of apoptosis. The CS-BP, GM-BP, and GM@CS-BP groups exhibited red fluorescence, and the RFI was close to that of the control group. A possible reason for this may have been that the BPQDs released from the hydrogel microsphere scaffold successfully blocked the peroxidation of the mitochondrial membrane by ROS, which is important for blocking the mitochondrial apoptotic pathway.

2.5. Regulation of ASIC and inflammation by GM@CS-BP

ASICs are cation channels directly activated by extracellular H^+. They not only participate in neural functions, such as touch,

nociception, learning, and memory, but are also involved in patho-physiological processes, such as inflammation, ischemia, and hypoxia. ASICs are involved in IVDD processes, which are characterized by NP cell reduction and ECM destruction (Fig. 5A) [8]. A recent study showed that ASIC-3 expression is significantly increased in degenerated NP cells. Extracellular acids activate downstream signaling pathways and regulate gene expression, stimulating the production of multiple pro-inflammatory factors such as TNF-α, IL-1β through the NF-κB signaling pathway [5]. This further enhances MMP activity and induces inflammation. In IVDs tissue, MMP13 is capable of specifically degrading COL-II, a major component of the ECM in IVDs. The imbalance between ECM synthesis and degradation is a major cause of IVDD. Therefore, using biomaterials to block the oxidative stress process, activation of ASICs, and onset of the downstream inflammatory cascade to promote the reconstruction of the ECM is an important therapeutic option for IVDs. In this study, the ability of GM@CS-BP microspheres to block ASIC-3 was assessed using immunofluorescent staining (Fig. 5C). In the H_2O_2 and GM groups, the expression of ASIC-3 was higher, whereas the CS-BP group was able to reduce the fluorescence intensity of ASIC-3 by 56%, compared to the H_2O_2 group (Fig. 5B). The GM@CS-BP microspheres were able to inhibit ASIC-3 fluorescence intensity by 49%, which demonstrated that the GM@CS-BP composite microspheres could negatively regulate ASIC-3 expression. The immunofluorescent staining of COL-II (Fig. 5D) showed that the expression of COL-II was increased by 85%, 63% and 79% in the CS-BP, GM-BP and GM@CS-BP groups,

respectively, compared to the control group (Fig. 5B, $p < 0.001$).

The semi-quantitative results of western blotting were as expected (Fig. 6A). The expression of ASIC-3 was significantly inhibited (Fig. 6B), whereas GM@CS-BP decreased the expression of pro-inflammatory factors such as TNF-α, cleaved IL-1β and IL-6 by 2.79-, 1.41 and 1.94-fold, respectively (Fig. 6C–E) and downregulated MMP13 synthesis (Fig. 6F). This reduced the degradation of the ECM in the NP cells, resulting in a 3.35-fold increase in COL-II (Fig. 6G). The quantitative real-time polymerase chain reaction (qRT-PCR) results (Figs. S5A–F) showed that the gene expression levels of ASIC-3, IL-1β, TNF-α, and IL-6 were significantly downregulated and that the expression of the catabolism-related gene MMP13 was reduced, while the expression of COL-II, a representative gene of the ECM in NP cells, was significantly increased. This further demonstrated that the ECM metabolic disorder caused by the chronic inflammatory response had improved. We further verified the activation of inflammation-related signaling pathways such as MAPK and NF-κB. The phosphorylation of p38 and p65 was inhibited by 1.78- and 1.53-fold in the GM@CS-BP group compared to the control group (Fig. 6H and I). Notably, CS-BP exhibits a similar effect to GM@CS-BP. These results demonstrate that the intervention of antioxidant BPQDs released from the oxygen metabolism-balanced engineered hydrogel microspheres or CS successfully attenuated the acidic environment-induced inflammatory cascade within the IVDs, thus reversing the imbalance of ECM synthesis and degradation. In conclusion, GM@CS-BP was able to regulate the oxidative stress
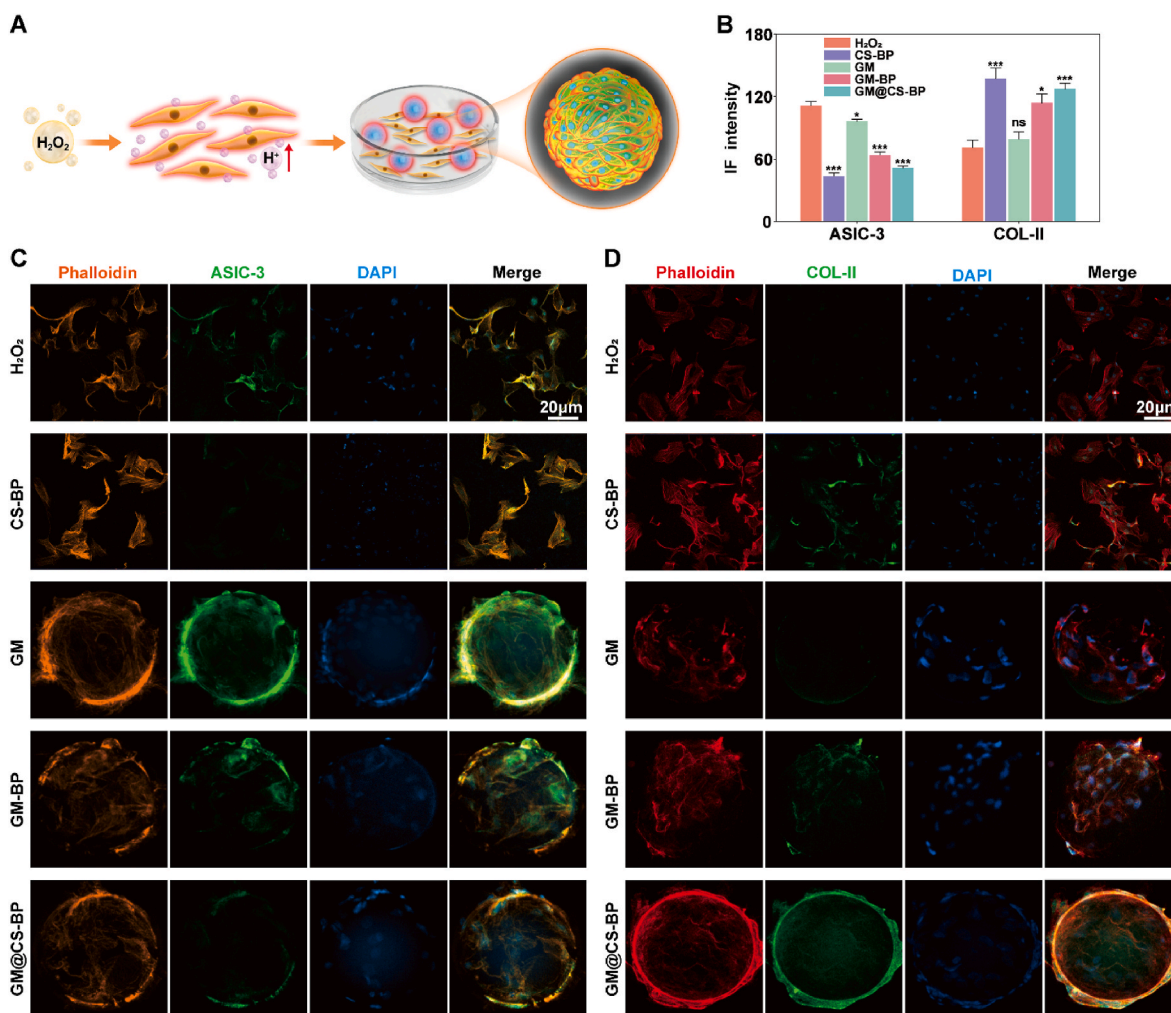

Fig. 5. A) Schematic diagram of cells co-cultured with microspheres after H_2O_2 intervention. B) Semiquantitative analysis of the immunofluorescent staining of ASIC-3 and COL-II. C–D) Immunofluorescence of ASIC-3 and COL-II. (n = 3; the results were compared with the control group by a one-way ANOVA and Tukey's test; *p < 0.05; ***p < 0.001).
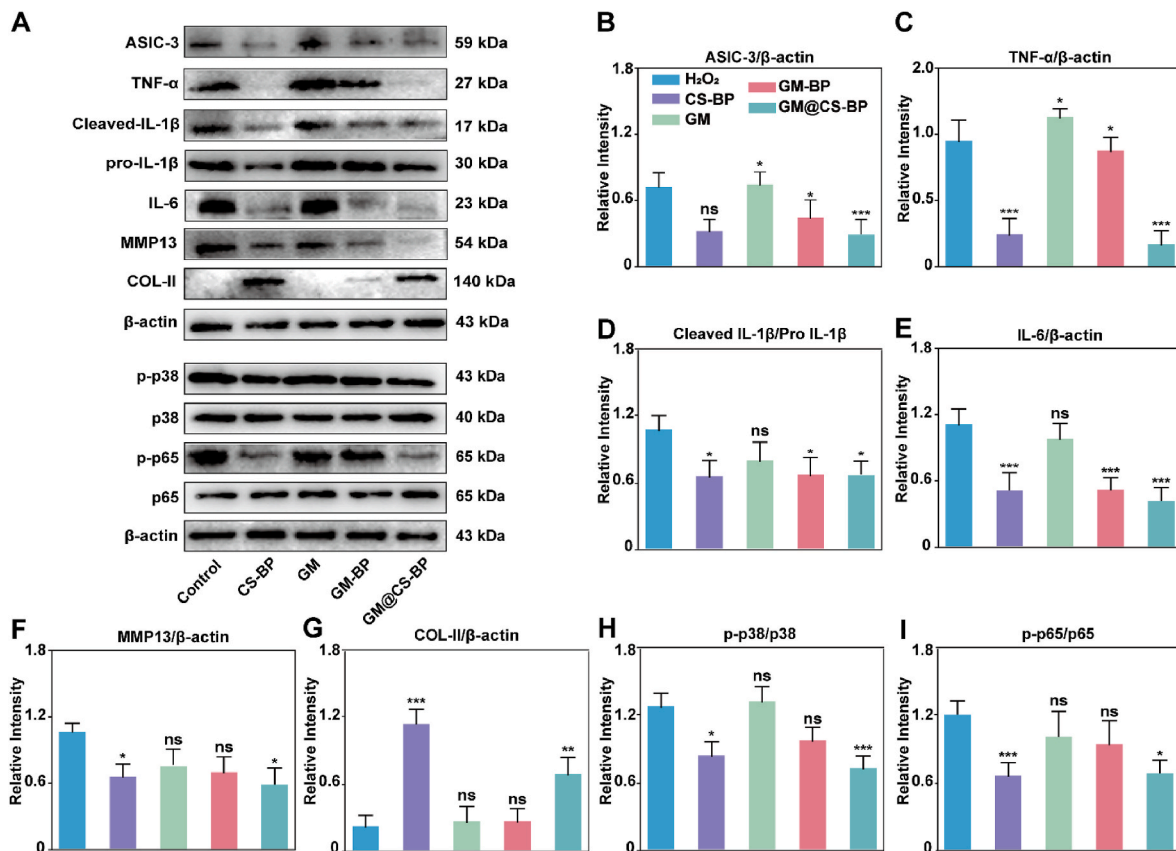
Fig. 6. Protein expression of NP cells following H_2O_2 stimulation. A) Western blot of ASIC-3, TNF-α, cleaved IL-1β, pro IL-1β, IL-6, MMP13, COL-II, and the NF-κB and p38 MAPK signaling pathways. B–G) Semiquantitative analysis of ASIC-3, TNF-α, cleaved IL-1β/pro IL-1β, IL-6, MMP13, and COL-II protein expression. H–I) Semiquantitative analysis of p65, p-p65, p38, and p-p38 protein expression. (n = 3; all data are presented as the mean ± standard deviation; *p < 0.05; **p < 0.01; ***p < 0.001; the comparisons between CS-BP, GM, GM-BP, GM@CS-BP, and the control group were performed by one-way ANOVAs and Tukey's test; ns, not significant).

microenvironment within the NP cells, providing proliferative capacities for the NP cells and successfully remodeling the ECMs of the NP by regulating local inflammation. However, IVDD is a complex and dynamic pathological microenvironment. The function of GM@CS-BP in neutralizing ROS, inhibiting the acid-sensing complex, and reducing the inflammatory response must be further explored *in vivo*.

2.6. In vivo anti-IVDD efficacy of GM@CS-BP microspheres

Improving the oxidative stress environment within IVDs and promoting the reconstruction of the ECM within NP *in vivo* were the ultimate aims of this study. To investigate the ability of oxygen metabolic balance-engineered hydrogel microspheres to delay IVDD *in vivo*, a rat caudal IVDD model was established (Fig. 7A) [39]. Imaging and histological sectioning are useful methods to assess IVDs degeneration and regeneration. As shown in Fig. 7B, there was a significant difference in disc height between the blank control and simple puncture groups at 4 and 8 weeks (Fig. 7D–E, p < 0.001). A significant decrease was observed at 8 weeks compared with that at 4 weeks, which proved the successful construction of the IVDD model. There was no significant difference between the CS-BP, GM and simple puncture groups at 4 and 8 weeks, whereas a significant recovery of disc height was observed in the GM-BP and GM@CS-BP groups compared to the CS-BP, GM and NC groups (p < 0.001). Owing to the long-term high pressure in the intervertebral disc, a large amount of leakage and loss occurred after the injection of nanoparticles, resulting in the CS-BP group performing worser in the *in vivo* experiment than in the *in vivo* experiment. A more significant increase in the GM@CS-BP group was observed compared to the GM-BP group (p < 0.05), indicating an improved loading rate and sustained release due to

the CS encapsulation of the BPQDs. The higher T2-weighted signal on the MRI scan indicated a higher water content in the NP (Fig. 7C). As IVDD progresses, the high loss of proteoglycans reduces the water content of the IVDs, which gradually "darken" in contrast to the healthy water-bearing tissue that appear white on MRI scans [38]. At 4 and 8 weeks, the NP of the NC group showed a significantly low T2-weighted signal (Fig. 7F), whereas the NP in the control group maintained a high-water content (p < 0.001), demonstrating irreversible damage after disc puncture. Compared to the CS-BP, GM and NC groups, a significant improvement in MRI grading based on the Thomson classification was found in the GM@CS-BP and GM-BP groups at 8weeks. The GM@CS-BP group showed improved MRI grading compared with the GM-BP group (p < 0.01). This further indicated that the BPQDs could regulate the local oxidative stress environment to repair the water content and collapse of IVDs and delay IVDD progression, whereas the introduction of CS further enhanced the repairing effects of the oxygen metabolic balance engineered hydrogel microspheres.

Tissue sections were collected 4 and 8 weeks after surgery. The morphology of the NP was observed using H&E staining (Fig. 8A) [61]. The NP area in the GM@CS-BP group was lower than that in the control group, but distinct tissue margins were observed. In contrast, the atrophy of the NP was not significantly improved in the GM group compared to the NC group, and the NP borders were difficult to distinguish. Although an NP area was observed in the GM-BP group, it was insufficient to represent NP regeneration. Safranin O/Fast green staining was used to assess the proteoglycan (orange) and collagen (blue) contents in the IVDs (Fig. 8B). The NP in the IVDs completely ruptured in the NC group and remained unimproved at 8 weeks. Significant orange aggregation was observed in the GM@CS-BP group compared to that in the
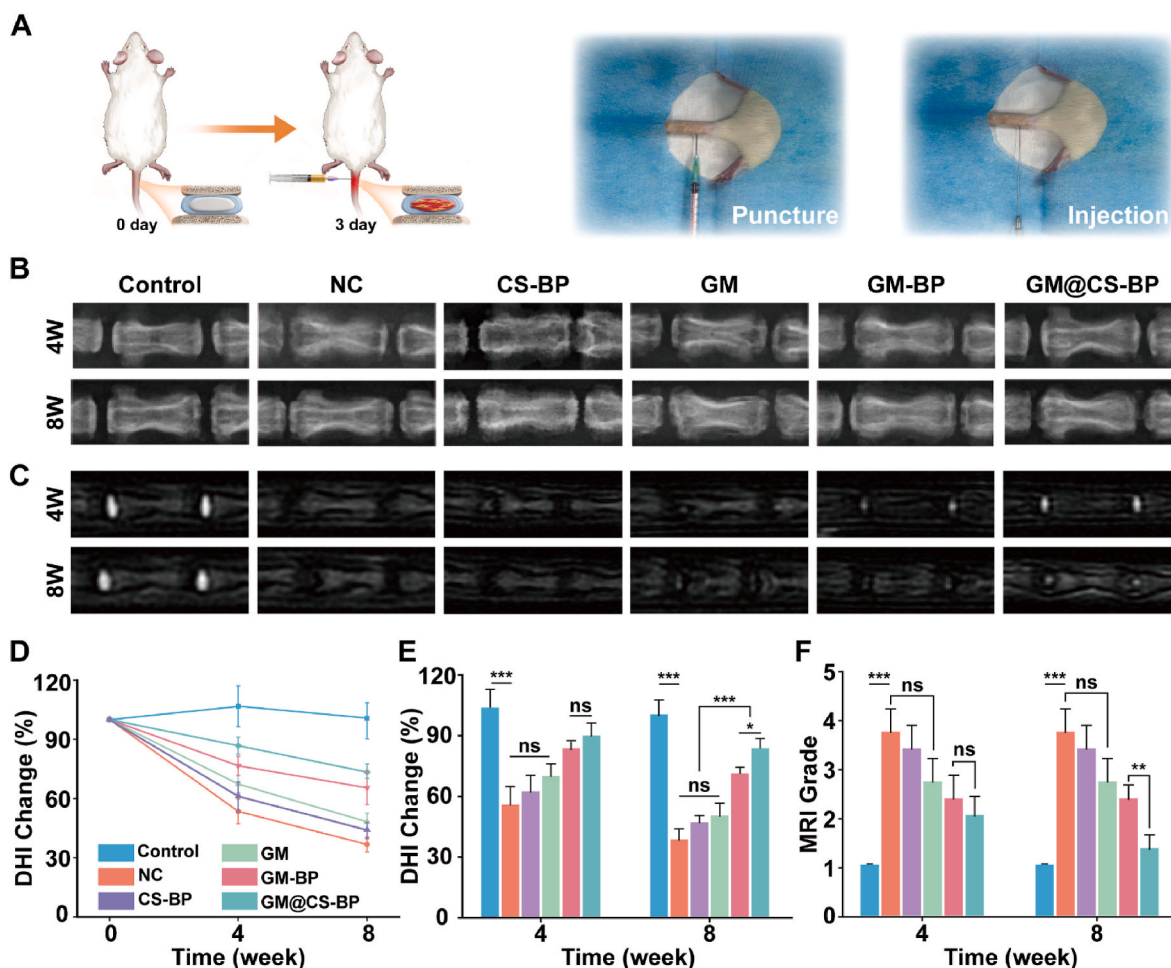
Fig. 7. Schematic diagram and MRI analysis of the IVDD model. A) Schematic diagram of the rat IVDD model and surgical photos. B) X-ray photos. C) MRI scans. D–E) DHI changes at 4 and 8 weeks. F) MRI grading 4 and 8 weeks after surgery. (n = 3; all data are presented as the mean ± standard deviation; *p < 0.05; **p < 0.01; ***p < 0.001; the comparison of NC, CS-BP, GM, GM-BP, and GM@CS-BP was performed by a one-way ANOVA and Tukey's test, respectively; ns, not significant).

NC group, indicating proteoglycan remodeling. Proteoglycans were observed in the GM-BP group but did not form an intact structure. They also did not lead to significant repairs in the degeneration or structural loss of the IVDs. At 4 and 8 weeks after surgery, the Masuda histological grading in the GM@CS-BP and GM-BP groups was significantly decreased compared to that in the NC, CS-BP and GM groups ($p < 0.001$) and further decreased with time, indicating the onset of regenerative processes (Fig. 8G). In addition, significantly enhanced repair was found in the GM@CS-BP group compared to the GM-BP group ($p < 0.05$). It was worth noting that although the anti-oxidation ability of the CS-BP group in the in vitro experiment was excellent, the therapeutic effect of CS-BP *in vivo* was limited. This may be because the IVDD is in a long-term high-pressure environment, and the excessive pressure load leads to continuous leakage and loss of nanoparticles, which ultimately leads to the inability of CS-BP to effectively play its biological role. This phenomenon was also observed in subsequent experiments. HO-1 is susceptible to induction by multiple stimuli, and the products yielded from the degradation of heme play an important protective role in cells. A slight increase in the intensity of HO-1 immunofluorescence was observed in the NC group compared to the control group (Fig. 8C), which was likely due to the oxidative stress environment activating the Nrf2/HO-1 pathway and triggering self-defense in the NP. The fluorescence intensity of HO-1 was significantly enhanced after treatment with GM-BP and GM@CS-BP compared to the simple puncture and GM groups, demonstrating that the composite microspheres were able to

upregulate HO-1 expression and attenuate oxidative stress-induced injury (Fig. 8H). To verify the ability of GM@CS-BP to block ROS-triggered ASIC activation and inhibit local ECM degradation, an immunohistochemical analysis of COL-II and ASIC-3 was performed (Fig. 8D, E). The immunofluorescent intensity of COL-II at 4 and 8 weeks was significantly enhanced in the GM@CS-BP group compared to the NC, GM, and GM-BP groups, and was 10.22- and 13.47-fold higher than that in the NC group, respectively (Fig. 8I). This indicated ECM remodeling induced by the slow sustained release of BPQDs from the material. The immunofluorescent intensity of ASIC-3 at 4 and 8 weeks in the GM@CS-BP group decreased by 1.91- and 4.31-fold compared to that in the NC group (Fig. 8J). ASIC-3 expression in the GM@CS-BP and GM-BP groups was significantly lower than that in the NC, CS-BP and GM groups at 4 weeks ($p < 0.001$). It was further found that ASIC-3 expression in the GM@CS-BP group was significantly inhibited compared to that in the GM ($p < 0.001$), NC ($p < 0.001$), and GM-BP ($p < 0.01$) groups at 8 weeks. Finally, we found that the immunofluorescent intensity of IL-1β (Fig. 8F) at 4 and 8 weeks in the GM@CS-BP group decreased by 2.45- and 3.87-fold, respectively, compared to that in the NC group (Fig. 8K). However, the CS-BP, GM and GM-BP groups were less effective than GM@CS-BP group. This may be due to the structure of GM@CS-BP, which can uniformly, effectively, and sustainably release antioxidant-type BPQDs and block the expression of acid-sensitive complexes by inhibiting oxidative stress, a trend that has become more significant over time. In summary, the *in vivo* results demonstrated
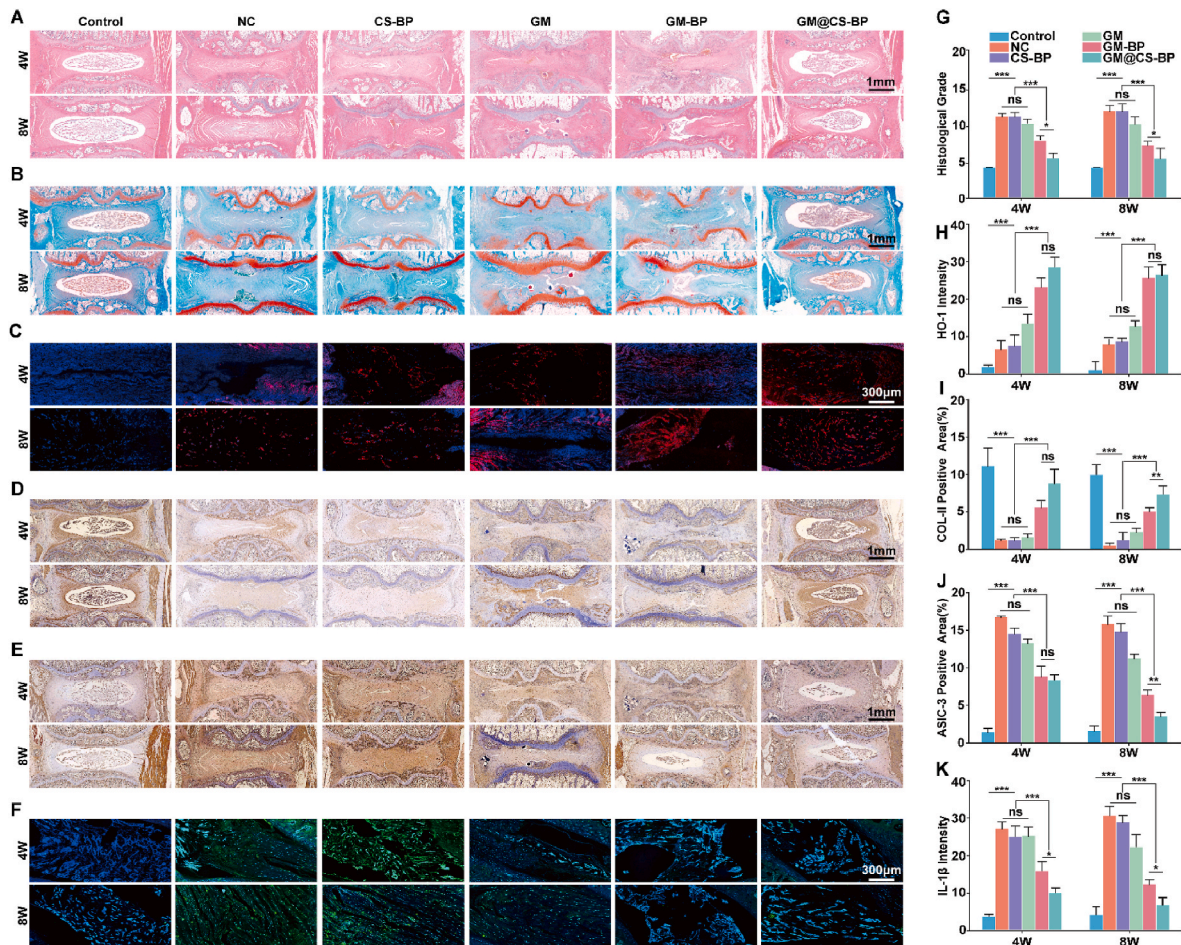
Fig. 8. Histological evaluation in vivo. A) H&E staining results at 4 weeks and 8 weeks. B) Safranin O-Fast Green staining. C) HO-1 immunofluorescence. D-E) COL-II and ASIC-3 immunohistochemical staining. F) IL-1β immunofluorescence. G) Histological grading at 4 weeks and 8 weeks. H) Semiquantitative analysis of HO-1 immunofluorescence. I-J) Semiquantitative analysis of COL-II and ASIC-3. K) Semiquantitative analysis of IL-1β immunofluorescence. (n = 3; all data are presented as mean ± standard deviation; *p < 0.05; **p < 0.01; ***p < 0.001; the comparison of NC, CS-BP, GM, GM-BP, GM@CS-BP in the blank control group and simple puncture group was performed by one-way ANOVA and Tukey's test, respectively; ns, not significant).

that although the disc height index (DHI%) and MRI signals in the GM-BP group were superior to those in the GM and NC groups, the GM@CS-BP group showed significantly better outcomes, and the improvements in DHI% and MRI signals were more pronounced after 8 weeks. Histological staining showed a significantly larger amount of residual NP tissue and proteoglycan deposition in the GM@CS-BP group, and the ROS-scavenging ability and HO-1 expression exceeded those of the other microspheres. Increased COL-II and decreased ASIC-3 intensities in the immunohistochemistry analyses also suggested that anti-ROS treatment could modulate the imbalance between ECM synthesis and degradation. The analyses further provided evidence for the inhibition of ASIC and blocking of the subsequent inflammatory cascade. These results demonstrate that the composite microspheres formed using GelMA microspheres and CS are capable of the sustained and targeted release of BPQDs into IVDs, inhibiting local overactive inflammatory responses, and promoting the regeneration of NP cells by blocking oxidative stress.

3. Conclusion

We found that ROS stimulation directly upregulated the expression of the ASIC-3 protein in NP cells and further activated the release of inflammatory factors, such as TNF-α and IL-1β. This not only proves that the imbalance of oxygen metabolism leads to the degradation of the ECM in NP tissue and accelerates IVDD, but also explores the positive

feedback between ROS and acid-sensitive complexes. These findings further provide new insights into anti-ROS therapy for IVDD. On this basis, novel oxygen metabolism-balanced engineered hydrogel microspheres were constructed to regulate the imbalance of ROS in IVDD precisely by the uniform loading and targeting and sustained release of strong antioxidant BPQDs from CS. The composite microspheres were found to downregulate the expression of the acid-sensing complex in NP cells under high-intensity ROS stimulation; block the activation of downstream inflammatory pathways; and block the vicious cycle between oxidative stress and inflammation to achieve ECM stability in IVDD, restore tissue function, and promote NP regeneration. The oxygen metabolism-balanced engineered hydrogel microspheres constructed in this study therefore represent a new approach for IVDD treatment through a local anti-oxidative stress strategy to regulate the expression of acid-sensing complexes.

4. Experimental section

4.1. Materials

All chemical reagents were purchased from Aladdin Reagent Co. (China) unless otherwise specified. Black phosphorus crystals were purchased from Xianfeng Nanomaterial Technology Co., Ltd. (China). Dulbecco's modified Eagle's medium (DMEM), fetal bovine serum (FBS), trypsin, and penicillin/streptomycin were purchased from Gibco

(USA).

4.2. Detection of lactate concentrations and pH

First, the NP cells were stimulated with different concentrations of H_2O_2 for 30 min, after which the cells were washed three times using DMEM/F12 medium and incubated in a cell incubator for 24 h. According to the manufacturer's instructions for the lactate detection kit (Sigma-Aldrich, lot:7G16K06070), a 1-nmol/µL lactate standard solution was prepared and used to plot the standard curve. The solution was then centrifuged and deproteinated using a 10-kDa MWCO spin filter to remove lactate dehydrogenase. The lactate concentration was measured using a colorimetric assay. The pH of the sample solution was determined using a pH microelectrode meter.

4.3. Western blot

The NP cells were stimulated with different concentrations (50, 100, 200, and 400 µM) of H_2O_2 for 30 min and then incubated for 24 h. The expression of the ASIC-3 (Abcam, ab49333) protein was detected by western blotting. Proteins were extracted by adding RIPA lysate containing a protease inhibitor. The protein concentration was quantified using a BCA protein quantification kit (Solarbio, China). After electrophoresis, membrane transfer, blocking, and incubation with the primary and secondary antibodies, the gel was scanned and photographed using a gel imaging system. The grayscale values of the bands in the images were quantified using ImageJ software.

4.4. Immunofluorescence detection of ROS-ASIC-3

The NP cells were treated with 0, 50, 100, 200, and 400 µM of H_2O_2 for 30 min, cultured for 24 h, fixed in 4% paraformaldehyde, and permeabilized with 0.3% Triton-X 100 (Sigma-Aldrich, USA). They were then incubated overnight with 5% bovine serum albumin (BSA; Biosharp, Shanghai, China) and the primary antibody against ASIC-3 (Novus Biologicals, NBP1-46288) overnight, washed, and then incubated with the secondary antibody at room temperature for 2 h. Phalloidin (Yearsen, China) and DAPI (Abcam, USA) were used for staining, and the cells were observed under an inverted fluorescence microscope. A semiquantitative fluorescence analysis was performed using ImageJ software.

4.5. In vivo experiments and animal screening

Male SD rats with an average weight of 300–350 g were purchased from Soochow University Laboratory Animal Center. Good surgical and therapeutic outcomes were achieved. This study was approved by the Ethics Committee of the First Affiliated Hospital of Soochow University.

4.6. Establishment of rat caudal IVDD models

The rats were injected intraperitoneally with 10% (wt%) chloral hydrate. After the rats had been anesthetized, their tails were sterilized. The rats were then continuously punctured with a needle in Co7–9 IVDs to induce degeneration. To ensure IVDD induction, the internal tissue of the IVDs was destroyed by suction after the needle punctures. Approximately 15 µL of the GM and GM@CS-BP microsphere solutions were injected using a micropump syringe and 15 µL of phosphate-buffered saline (PBS) were injected into the NC group. After surgery, the rats were placed in a warm and ventilated area.

4.7. Radiographic evaluations using X-rays and MRI

Four and eight weeks after the surgeries, three rats were randomly selected from each group and underwent X-rays and MRI before being sacrificed. Each rat was placed in the supine position, and its tail was placed on a mammography device. The acquired X-ray images were assessed using ImageJ software, and the DHI% was calculated. MRI was performed using a 1.5T system (GE). T2-weighted images were acquired in the coronal plane. Radiologists who were blinded to the grouping assessed the T2-weighted signal intensities and scored the MRI with grades from I to IV according to the modified Thomson classification.

4.8. Histological evaluation, immunofluorescence, and immunohistochemistry

Four and eight weeks after the surgeries, the rats were sacrificed, and the IVDs were removed and immersed in formalin. They were decalcified in 10% EDTA for 30 days and embedded in paraffin. The specimens were sectioned at a thickness of approximately 5 µm. The changes in tissue structure and collagen within the discs were observed by H&E staining and Safranin O/Fast green staining, respectively. Histological grading was performed using the scale established by Masuda et al. (Table S2), which was scored from 4 (normal) to 12 (severe degeneration). Immunohistochemical staining for COL-II (ab34712), and ASIC-3 (Novus Biologicals, NBP1-46288), HO-1 (Servicebio, GB11104) and IL-1β (ab283818) fluorescence was also performed on the sections for comparison with the NC group.

4.9. Preparation of BPQDs

The BPQDs were prepared using the established liquid-phase exfoliation technique (the process was carried out under nitrogen protection). First, 20 mg of BP crystals were dispersed in 20 mL of N-methyl-2-pyrrolidone (NMP) solution and sonicated in an ice water bath at 1200 W for 3 h (Nanjing Saifei Co., Ltd., China; ultrasonic frequency: 19–25 kHz, 2 s on/3 s off), after which the obtained solution was sonicated again in an ice water bath for 12 h. The dispersion was centrifuged at 7000 rpm for 20 min to remove undispersed BP. The supernatant was collected in a new tube and centrifuged at 15,000 rpm for 2 h. After centrifugation, the supernatant was discarded, and the residue was resuspended in deionized water.

4.10. Preparation of CS-BPQDs

CS (40 mg, 200–400 mPa s) was dissolved in 20 mL of 1% (w/v) acetic acid solution at room temperature with magnetic stirring. When the solvent was clear and transparent, the pH was adjusted to 5.0 using a 10 M NaOH solution and filtered three times with a 0.45-µm filter membrane (to prepare the CS-BPQDs, the BPQDs (0.2 mg/mL) were resuspended in CS nanoparticles with a BPQDs/CS mass ratio of 1:10). Trimeric phosphate (TPP) solution (0.7 mg/mL) was then added dropwise under magnetic stirring at 720 rpm to achieve a CS/TPP mass ratio of 4:1. At this point, the solution produced a transparent, opalescent color, indicating that TPP and CS had undergone ion crosslinking polymerization. The solution was then sonicated for 5 min using an ultrasonic crusher with 900 W power. This was repeated 2–3 times. The obtained CS nanoparticles were then filtered through a 0.22-µm filter membrane three times.

4.11. Preparation of GelMA

First, 20 g of gelatin were weighed in 200 mL of PBS, placed in a water bath, and stirred at 60 °C for 1 h until complete dissolution to obtain a 10% (w/v) transparent yellowish gelatin solution. Subsequently, 16 mL of MA were added dropwise to the gelatin solution using a micropump at a rate of 0.25 mL/min under light-proof conditions. The solution was then stirred continuously at 60 °C for 2 h, 800 mL of preheated PBS were added to the above reaction, and stirring was continued for 15 min. The solution was then dialyzed in 12–14-kDa dialysis bags for 2 weeks. The PBS was replaced every 2 days to obtain the GelMA solution, which was freeze-dried and stored in a −80 °C refrigerator.

4.12. Preparation of GelMA hydrogel microspheres and GM-BP

The GelMA hydrogel microspheres were prepared using a water-in-oil microfluidic technique. First, coaxial electrospinning nozzles (inner and outer needles with diameters of 30G and 21G, respectively) were connected to two micropumps through silicone tubes. The outer needle of the coaxial electrospinning nozzle was used as a continuous phase for co-flow shearing and was connected to an isopropyl myristate solution containing 10% (w/w) Span80. The inner needle was connected to the dispersed phase with a 7% (w/v) GelMA aqueous solution and 0.5% (w/v) I2595 photoinitiator. The flow rate of the aqueous (GelMA) phase to the oil phase was adjusted to 15:500 μL/min by adjusting the micropump. Continuous monodisperse spherical microdroplets were produced at the interface. After the droplets were uniform in size, they were placed in a beaker with a prefilled oil solution under light-proof conditions. The beaker was removed every 10–20 min, fully irradiated with UV light, and replaced (the entire system was maintained at a certain temperature to prevent cross-linking blockage in the needle). The collected cross-linked hydrogel microspheres were then washed three times with 75% ethanol and five times with PBS. The PBS was then changed every 3 h to remove the photoinitiator and oil. The purified microspheres were frozen overnight at −80 °C and freeze-dried immediately after removal to obtain porous hydrogel microspheres. The prepared freeze-dried GelMA microsphere redissolved-solution was blended with 1.25 mL BPQDs solution (0.2 mg/mL) and stirred at 37 °C for 5 min under nitrogen protection.

4.13. Grafting of microspheres with nanoparticles and concentration screening

Lyophilized microspheres, 16 mg of EDC, and 24 mg of NHS were added sequentially to 2 mL of MES buffer (pH 6.0). The cells were then activated in a thermostatic shaker at 37 °C for 15 min. The prepared CS-BP solution was added to the microspheres in different volumes so that the volume ratios of the CS-BP to microsphere solutions were 1:1, 1:2, 1:4, 1:8, and 1:16. They were incubated overnight at 37 °C in a thermostatic shaker, centrifuged, and rinsed three times with deionized water. To explore the microsphere-to-nanoparticle volume ratio that possesses the most suitable ROS-scavenging capacity, approximately 200 of the obtained purified microspheres were placed in 24-well plates, sterilized with alcohol and UV, washed three times with PBS, and soaked in culture medium for 6 h. Approximately 4×10^4 of the NP cells stimulated with 200 μM of H_2O_2 were inoculated into microspheres and co-cultured overnight. DCFH-DA fluorescent probes were diluted in serum-free medium at 1:1000. The microsphere–cell co-culture system was washed with PBS, and an appropriate volume of diluted DCFH-DA fluorescent probes was added and incubated in a 37 °C cell incubator for 30 min. Morphological observations were made by fluorescence microscopy and semiquantitative fluorescence analyses using ImageJ software.

4.14. Nanoparticle and microsphere characterization

The particle sizes and Zeta potentials of the CS nanoparticles were measured using a Zetasizer (Malvern Zetasizer Nano zs90, UK). The morphologies of the CS nanoparticles, BPQDs, and CS-BP were examined by TEM (Hitachi HT7700, Japan) at 200 kV. The GelMA and GM@CS-BP microspheres were immobilized using a conductive adhesive and plated with gold for 45 s (Quorum Technologies, SC7620, UK). The morphologies were observed by scanning electron microscopy (SEM; Hitachi S-4800 SEM, Japan) at an accelerating voltage of 10 kV. A surface elemental analysis of the microspheres was performed using EDS (Oxford), and the elemental compositions of the microspheres, nanoparticles, and BPQDs were examined using IR (Thermo Scientific, Nicolet 6700, USA) and Raman spectroscopy (Renishaw, InVia Spectrometer).

4.15. Encapsulation and release efficiency measurements of composite microspheres

The constructed CS-BP, GM-BP, and GM@CS-BP (the volume ratio of the GM microsphere solution to CS-BP nanoparticle solution was 4:1) were prepared according to Sections 4.10, 4.12, and 4.13, respectively, and free BPQDs in the suspension were collected after centrifugation at 1400 rpm for 5 min. The mass of BPQDs was calculated (W1) using an inductively coupled plasma emission spectrometer (7400 DUO, Thermo Fisher), the total amount of phosphorus was 0.25 mg (W2), and the encapsulation efficiency was calculated according to Equation (1). The samples were prepared in triplicates. The remaining materials were placed in 10 mL of pure water in a 37 °C thermostatic shaker at 100 rpm. The supernatant was collected after 1, 2, 3, 5, 7, 9, 12, 15, 18, and 21 days and resuspended in 10 mL of pure water (under nitrogen protection). The obtained supernatants were analyzed using ICP to determine the concentration of elemental phosphorus in each solution.

$$\text{Encapsulation efficiency} = \frac{W2 - W1}{W2} \times 100\% \qquad \text{Equation (1)}$$

4.16. Preparation for the in vitro experiments

The NP cells used in the experiments were extracted from the caudal vertebrae of the SD rats. The rat caudal vertebrae were isolated under aseptic conditions. The NP tissue at each stage was finely removed using ophthalmic forceps; 0.25% type II collagenase was added; and the cells were incubated in a 37 °C cell culture incubator for 2 h. The cell suspension was filtered using a cell filter. The supernatant was discarded by centrifugation, and DMEM/F12 medium with 10% FBS was added after three washes with sterile PBS. The cells were incubated in a cell culture incubator at 37 °C with 5% CO_2. The medium was changed every 2–3 days, and the cells were passaged or frozen for approximately 1 week.

4.17. Co-culture of microspheres and cells and screening of H_2O_2 concentrations

Approximately 200 of the obtained purified microspheres were placed into 24-well plates, sterilized with alcohol and UV, washed three times with PBS, and soaked in microspheres for 6 h. Approximately 4×10^4 of the NP cells, which had been pre-stimulated with 0, 50, 100, 200, and 400 μM of H_2O_2 for 30 min, were inoculated into the microspheres and co-cultured overnight. Incubation was continued in a cell incubator at 37 °C for 6 and 24 h. The CCK-8 assay kit (Dojindo, Japan) was added to the medium at 10% (v/v) for 4 h. The medium (100 μL) was transferred into 96-well plates. Absorbance was measured at 450 nm using an enzyme marker.

4.18. Total antioxidant capacity of the materials

Approximately 200 GM, GM-BP, GM@CS-BP microspheres and CS-BP were resuspended in 2 mL of PBS. After 6 h, the supernatant was collected according to the manufacturer's instructions for the T-AOC assay kit (Beyotime, Shanghai, China). The Trolox-equivalent antioxidant capacity was determined using the 2,2′-azido bis (3-ethyl-benzothiazoline-6-sulfonic acid) method and was presented in mmol/L.

4.19. Cell viability

A live/dead staining assay was performed. After 4 and 7 days of co-culturing the microspheres and cells, live/dead kits (Invitrogen, USA) were added to 24-well plates and incubated for 30 min at room temperature. Cell morphology was observed using an inverted fluorescence microscope.

4.20. Immunofluorescence

The microspheres and cells were co-cultured using a previously described method and intervened with 200 μM of H_2O_2. After being cultured for 3 days, they were incubated overnight with primary antibodies against ASIC-3 and COL-II. They were then fixed, permeabilized, blocked, washed, and incubated with secondary antibodies at room temperature for 2 h. They were stained with phalloidin (Yearsen, China) and DAPI (Abcam, USA) and were then observed by confocal microscopy. A semiquantitative fluorescence analysis was performed using ImageJ software.

4.21. Mitochondrial membrane potential

The microsphere–cell co-culture system was established using the above method. JC-1 staining working solution was prepared according to the manufacturer's instructions for the JC-1 kit (Solarbio, China). An appropriate amount of working solution was added and incubated in a 37 °C cell incubator for 20 min. The solution was then washed twice with JC-1 staining buffer and culture medium. An inverted fluorescence microscope was used to observe the staining, and ImageJ software was used for the semiquantitative fluorescence analysis.

4.22. Western blot

Based on the above co-culture system, incubation was continued for 4 days after stimulation with 200 μM of H_2O_2. The protein expression of ASIC-3, IL-1β (ab9722), IL-6 (ab9324), TNF-α (ab66579), MMP-13 (ab39012), COL-II (ab34712), p65 (ab16502), p-p65 (ab28856), p38 (ab31828), p-p38 (ab45381), and GAPDH (ab8245) was measured by western blotting. The images were assessed using ImageJ for a gray value analysis of the bands.

4.23. qRT-PCR analysis

Based on the above co-culture system, incubation was continued for 4 days after stimulation with 200 μM of H_2O_2. The gene expression of COL-II, ASIC-3, IL-1β, TNF-α, IL-6, MMP-13, and GAPDH in GM, GM-BP, and GM@CS-BP was detected by qRT-PCR. Primer sequences were designed using Genewiz and are summarized in Table S3 as supporting information.

4.24. Statistical analysis

All data are expressed as the mean ± standard deviation. Statistical analyses and images were processed using Origin and assessed using a one- or two-way ANOVA. Tukey's multiple comparisons test was used to further assess the differences between the groups (n = 3; *$p < 0.05$; **$p < 0.01$; ***$p < 0.001$; ns, not significant).

CRediT authorship contribution statement

Ziang Li: Conceptualization, Methodology, Investigation, Formal analysis, Data curation, Writing – original draft. **Feng Cai:** Methodology, Investigation, Formal analysis, Resources. **Jincheng Tang:** Conceptualization, Methodology, Formal analysis, Writing – review & editing. **Yichang Xu:** Conceptualization, Methodology, Formal analysis, Data curation, Writing – original draft, Writing – review & editing-revised manuscript. **Kaijin Guo:** Formal analysis, Supervision. **Zonghan Xu:** Investigation, Formal analysis. **Yu Feng:** Formal analysis, Data curation. **Kun Xi:** Formal analysis, Writing – review & editing, Supervision, Funding acquisition. **Yong Gu:** Conceptualization, Methodology, Supervision, Funding acquisition. **Liang Chen:** Conceptualization, Methodology, Writing – review & editing, Supervision, Funding acquisition.

Appendix A. Supplementary data

Supplementary data to this article can be found online at https://doi.org/10.1016/j.bioactmat.2022.12.025.

References

[1] A. Dimozi, E. Mavrogonatou, A. Sklirou, D. Kletsas, Oxidative stress inhibits the proliferation, induces premature senescence and promotes a catabolic phenotype in human nucleus pulposus intervertebral disc cells, Eur. Cell. Mater. 30 (2015) 89–102, discussion 103.

[2] L. Li, J. Guo, Y. Wang, X. Xiong, H. Tao, J. Li, Y. Jia, H. Hu, J. Zhang, A broad-spectrum ROS-eliminating material for prevention of inflammation and drug-induced organ toxicity, Adv. Sci. 5 (10) (2018), 1800781.

[3] D. Yang, D. Wang, A. Shimer, F. Shen, X. Li, X. Yang, Glutathione protects human nucleus pulposus cells from cell apoptosis and inhibition of matrix synthesis, Connect. Tissue Res. 55 (2) (2014) 132–139.

[4] L. Dada, J. Sznajder, Mitochondrial Ca(2+) and ROS take center stage to orchestrate TNF-alpha-mediated inflammatory responses, J. Clin. Invest. 121 (5) (2011) 1683–1685.

[5] H. Blaser, C. Dostert, T. Mak, D. Brenner, TNF and ROS crosstalk in inflammation, Trends Cell Biol. 26 (4) (2016) 249–261.

[6] D. Seol, M. Coleman, J. Martin, I. Song, L. Jaidev, A. Salem, T.H. Lim, Targeting oxidative stress with amobarbital to prevent intervertebral disc degeneration: Part I. in vitro and ex vivo studies, Spine J. 21 (6) (2021) 1021–1030.

[7] B. Wu, J. Bargaineer, L. Zhang, T. Yang, Z. Xiong, T. Leng, Upregulation of acid sensing ion channel 1a (ASIC1a) by hydrogen peroxide through the JNK pathway, Acta Pharmacol. Sin. 42 (8) (2021) 1248–1255.

[8] F. Cai, X. Hong, X. Tang, N. Liu, F. Wang, L. Zhu, X. Xie, Z. Xie, X. Wu, ASIC1a activation induces calcium-dependent apoptosis of BMSCs under conditions that mimic the acidic microenvironment of the degenerated intervertebral disc, Biosci. Rep. 39 (11) (2019).

[9] K. Zhao, R. An, Q. Xiang, G. Li, K. Wang, Y. Song, Z. Liao, S. Li, W. Hua, X. Feng, X. Wu, Y. Zhang, A. Das, C. Yang, Acid-sensing ion channels regulate nucleus pulposus cell inflammation and pyroptosis via the NLRP3 inflammasome in intervertebral disc degeneration, Cell Prolif 54 (1) (2021), e12941.

[10] R. Qin, S. Dai, X. Zhang, H. Liu, B. Zhou, P. Zhou, C. Hu, Danshen attenuates intervertebral disc degeneration via antioxidation in SD rats, Oxid. Med. Cell. Longev. (2020), 6660429, 2020.

[11] A. Mostert, Melanin, the what, the why and the how: an introductory review for materials scientists interested in flexible and versatile polymers, Polymers 13 (10) (2021).

[12] S. Suzuki, N. Fujita, N. Hosogane, K. Watanabe, K. Ishii, Y. Toyama, K. Takubo, K. Horiuchi, T. Miyamoto, M. Nakamura, M. Matsumoto, Excessive reactive oxygen species are therapeutic targets for intervertebral disc degeneration, Arthritis Res. Ther. 17 (2015) 316.

[13] Z. Liao, H. Liu, L. Ma, J. Lei, B. Tong, G. Li, W. Ke, K. Wang, X. Feng, W. Hua, S. Li, C. Yang, Engineering extracellular vesicles restore the impaired cellular uptake and attenuate intervertebral disc degeneration, ACS Nano 15 (9) (2021) 14709–14724.

[14] Z. Liao, S. Li, S. Lu, H. Liu, G. Li, L. Ma, R. Luo, W. Ke, B. Wang, Q. Xiang, Y. Song, X. Feng, Y. Zhang, X. Wu, W. Hua, C. Yang, Metformin facilitates mesenchymal stem cell-derived extracellular nanovesicles release and optimizes therapeutic efficacy in intervertebral disc degeneration, Biomaterials 274 (2021), 120850.

[15] K. Xi, Y. Gu, J. Tang, H. Chen, Y. Xu, L. Wu, F. Cai, L. Deng, H. Yang, Q. Shi, W. Cui, L. Chen, Microenvironment-responsive immunoregulatory electrospun fibers for promoting nerve function recovery, Nat. Commun. 11 (1) (2020) 4504.

[16] Y. Han, J. Yang, W. Zhao, H. Wang, Y. Sun, Y. Chen, J. Luo, L. Deng, X. Xu, W. Cui, H. Zhang, Biomimetic injectable hydrogel microspheres with enhanced lubrication and controllable drug release for the treatment of osteoarthritis, Bioact. Mater. 6 (10) (2021) 3596–3607.

[17] N. Kong, X. Ji, J. Wang, X. Sun, G. Chen, T. Fan, W. Liang, H. Zhang, A. Xie, O. C. Farokhzad, W. Tao, ROS-mediated selective killing effect of black phosphorus: mechanistic understanding and its guidance for safe biomedical applications, Nano Lett. 20 (5) (2020) 3943–3955.

[18] N. Wang, N. Mao, Z. Wang, X. Yang, X. Zhou, H. Liu, S. Qiao, X. Lei, J. Wang, H. Xu, X. Ling, Q. Zhang, Q. Feng, J. Kong, Electrochemical delamination of ultralarge few-layer black phosphorus with a hydrogen-free intercalation mechanism, Adv. Mater. 33 (1) (2021), e2005815.

[19] Y. Miao, X. Shi, Q. Li, L. Hao, L. Liu, X. Liu, Y. Chen, Y. Wang, Engineering natural matrices with black phosphorus nanosheets to generate multi-functional therapeutic nanocomposite hydrogels, Biomater. Sci. 7 (10) (2019) 4046–4059.

[20] Z. Zhang, P. Zhang, S. Yang, T. Zhang, M. Loffler, H. Shi, M.R. Lohe, X. Feng, Oxidation promoted osmotic energy conversion in black phosphorus membranes, Proc. Natl. Acad. Sci. U. S. A. 117 (25) (2020) 13959–13966.

[21] W. Chen, J. Ouyang, X. Yi, Y. Xu, C. Niu, W. Zhang, L. Wang, J. Sheng, L. Deng, Y. N. Liu, S. Guo, Black phosphorus nanosheets as a neuroprotective nanomedicine for neurodegenerative disorder therapy, Adv. Mater. 30 (3) (2018).

[22] J. Hou, H. Wang, Z. Ge, T. Zuo, Q. Chen, X. Liu, S. Mou, C. Fan, Y. Xie, L. Wang, Treating acute kidney injury with antioxidative black phosphorus nanosheets, Nano Lett. 20 (2) (2020) 1447–1454.

[23] Y. Zhang, C. Ma, J. Xie, H. Agren, H. Zhang, Black phosphorus/polymers: status and challenges, Adv. Mater. 33 (37) (2021), e2100113.

[24] J. Liu, P. Du, T. Liu, B.J. Cordova Wong, W. Wang, H. Ju, J. Lei, A black phosphorus/manganese dioxide nanoplatform: oxygen self-supply monitoring, photodynamic therapy enhancement and feedback, Biomaterials 192 (2019) 179–188.

[25] J. Yang, Y. Zhu, F. Wang, L. Deng, X. Xu, W. Cui, Microfluidic liposomes-anchored microgels as extended delivery platform for treatment of osteoarthritis, Chem. Eng. J. 400 (2020).

[26] M. Qu, X. Liao, N. Jiang, W. Sun, W. Xiao, X. Zhou, A. Khademhosseini, B. Li, S. Zhu, Injectable open-porous PLGA microspheres as cell carriers for cartilage regeneration, J. Biomed. Mater. Res. 109 (11) (2021) 2091–2100.

[27] W. Pan, C. Dai, Y. Li, Y. Yin, L. Gong, J.O. Machuki, Y. Yang, S. Qiu, K. Guo, F. Gao, PRP-chitosan thermoresponsive hydrogel combined with black phosphorus nanosheets as injectable biomaterial for biotherapy and phototherapy treatment of rheumatoid arthritis, Biomaterials 239 (2020), 119851.

[28] Z. Li, G. Luo, W. Hu, J. Hua, S. Geng, P. Chu, J. Zhang, H. Wang, X. Yu, Mediated drug release from nanovehicles by black phosphorus quantum dots for efficient therapy of chronic obstructive pulmonary disease, Angew Chem. Int. Ed. Engl. 59 (46) (2020) 20568–20576.

[29] S. Wan, B. Zhang, S. Li, B. He, Y. Pu, Combination of PEG-decorated black phosphorus nanosheets and immunoadjuvant for photoimmunotherapy of melanoma, J. Mater. Chem. B 8 (14) (2020) 2805–2813.

[30] M. Risbud, I. Shapiro, Role of cytokines in intervertebral disc degeneration: pain and disc content, Nat. Rev. Rheumatol. 10 (1) (2014) 44–56.

[31] A. Sinkemani, F. Wang, Z. Xie, L. Chen, C. Zhang, X. Wu, Nucleus pulposus cell conditioned medium promotes mesenchymal stem cell differentiation into nucleus pulposus-like cells under hypoxic conditions, Stem Cell. Int. (2020), 8882549, 2020.

[32] Y. Wang, Y. Zhang, K. Chen, F. Shao, Y. Wu, C. Guo, H. Wu, D. Zhang, W. Li, Q. Kong, H. Wang, Injectable nanostructured colloidal gels resembling native nucleus pulposus as carriers of mesenchymal stem cells for the repair of degenerated intervertebral discs, Mater Sci Eng C Mater Biol Appl 128 (2021), 112343.

[33] C. Cunha, C. Leite Pereira, J. Ferreira, C. Ribeiro-Machado, S. Grad, S. Santos, R. Goncalves, Therapeutic strategies for IVD regeneration through hyaluronan/ SDF-1-based hydrogel and intravenous administration of MSCs, Int. J. Mol. Sci. 22 (17) (2021).

[34] Y. Gan, P. Li, L. Wang, X. Mo, L. Song, Y. Xu, C. Zhao, B. Ouyang, B. Tu, L. Luo, L. Zhu, S. Dong, F. Li, Q. Zhou, An interpenetrating network-strengthened and toughened hydrogel that supports cell-based nucleus pulposus regeneration, Biomaterials 136 (2017) 12–28.

[35] V. Sanna, A. Roggio, N. Pala, S. Marceddu, G. Lubinu, A. Mariani, M. Sechi, Effect of chitosan concentration on PLGA microspheres for controlled release and stability of resveratrol, Int. J. Biol. Macromol. 72 (2015) 531–536.

[36] B. Li, F. Wang, F. Hu, T. Ding, P. Huang, X. Xu, J. Liang, C. Li, Q. Zhou, M. Lu, L. Deng, L. Guo, W. Cui, Injectable "nano-micron" combined gene-hydrogel microspheres for local treatment of osteoarthritis, NPG Asia Mater. 14 (1) (2022).

[37] S. Ding, X. Liu, X. Zhao, K. Wang, W. Xiong, Z. Gao, C. Sun, M. Jia, C. Li, Q. Gu, M. Zhang, Microcarriers in application for cartilage tissue engineering: recent progress and challenges, Bioact. Mater. 17 (2022) 81–108.

[38] J. Bian, F. Cai, H. Chen, Z. Tang, K. Xi, J. Tang, L. Wu, Y. Xu, L. Deng, Y. Gu, W. Cui, L. Chen, Modulation of local overactive inflammation via injectable hydrogel microspheres, Nano Lett. 21 (6) (2021) 2690–2698.

[39] Y. Xu, Y. Gu, F. Cai, K. Xi, T. Xin, J. Tang, L. Wu, Z. Wang, F. Wang, L. Deng, C. L. Pereira, B. Sarmento, W. Cui, L. Chen, Metabolism balance regulation via antagonist-functionalized injectable microsphere for nucleus pulposus regeneration, Adv. Funct. Mater. 30 (52) (2020).

[40] S. Zhang, B. Hu, W. Liu, P. Wang, X. Lv, S. Chen, Z. Shao, The role of structure and function changes of sensory nervous system in intervertebral disc-related low back pain, Osteoarthritis Cartilage 29 (1) (2021) 17–27.

[41] I. Kushkevych, D. Dordevic, P. Kollar, M. Vitezova, L. Drago, Hydrogen sulfide as a toxic product in the small-large intestine Axis and its role in IBD development, J. Clin. Med. 8 (7) (2019).

[42] K. Masuda, Y. Aota, C. Muehleman, Y. Imai, M. Okuma, E. Thonar, G. Andersson, H. An, A novel rabbit model of mild, reproducible disc degeneration by an anulus needle puncture: correlation between the degree of disc injury and radiological and histological appearances of disc degeneration, Spine 30 (1) (2005) 5–14.

[43] R. Wang, D. Luo, Z. Li, H. Han, Dimethyl fumarate ameliorates nucleus pulposus cell dysfunction through activating the Nrf2/HO-1 pathway in intervertebral disc degeneration, Comput. Math. Methods Med. (2021) 6021763, 2021.

[44] H. Wang, X. Yang, W. Shao, S. Chen, J. Xie, X. Zhang, J. Wang, Y. Xie, Ultrathin black phosphorus nanosheets for efficient singlet oxygen generation, J. Am. Chem. Soc. 137 (35) (2015) 1376–11382.

[45] X. Zhang, H. Xie, Z. Liu, C. Tan, Z. Luo, H. Li, J. Lin, L. Sun, W. Chen, Z. Xu, L. Xie, W. Huang, H. Zhang, Black phosphorus quantum dots, Angew Chem. Int. Ed. Engl. 54 (12) (2015) 3653–3657.

[46] E. Szliszka, Z.P. Czuba, M. Domino, B. Mazur, G. Zydowicz, W. Krol, Ethanolic extract of propolis (EEP) enhances the apoptosis- inducing potential of TRAIL in cancer cells, Molecules 14 (2) (2009) 738–754.

[47] H. Zhang, M. Oh, C. Allen, E. Kumacheva, Monodisperse chitosan nanoparticles for mucosal drug delivery, Biomacromolecules 5 (6) (2004) 2461–2468.

[48] S. Debnath, R.S. Kumar, M. Babu, Ionotropic gelation - a novel method to prepare chitosan nanoparticles, Res. J. Pharm. Technol. 4 (4) (2011) 492–495.

[49] L. Cheng, Z. Chen, Z. Cai, J. Zhao, M. Lu, J. Liang, F. Wang, J. Qi, W. Cui, L. Deng, Bioinspired functional black phosphorus electrospun fibers achieving recruitment and biomineralization for staged bone regeneration, Small 16 (50) (2020), e2005433.

[50] A. Pandey, A. Nikam, G. Fernandes, S. Kulkarni, B. Padya, R. Prassl, S. Das, A. Joseph, P.K. Deshmukh, P.O. Patil, S. Mutalik, Black phosphorus as multifaceted advanced material nanoplatforms for potential biomedical applications, Nanomaterials 11 (1) (2020).

[51] F. Wang, L. Nan, S. Zhou, Y. Liu, Z. Wang, J.C. Wang, X. Feng, L. Zhang, Injectable hydrogel combined with nucleus pulposus-derived mesenchymal stem cells for the treatment of degenerative intervertebral disc in rats, Stem Cell. Int. (2019), 8496025, 2019.

[52] Y. Jo, D. Lee, Biopolymer microparticles prepared by microfluidics for biomedical applications, Small 16 (9) (2020), e1903736.

[53] K. Modaresifar, A. Hadjizadeh, H. Niknejad, Design and fabrication of GelMA/ chitosan nanoparticles composite hydrogel for angiogenic growth factor delivery, Artif. Cell Nanomed. Biotechnol. 46 (8) (2018) 1799–1808.

[54] J. Chen, D. Huang, L. Wang, J. Hou, H. Zhang, Y. Li, S. Zhong, Y. Wang, Y. Wu, W. Huang, 3D bioprinted multiscale composite scaffolds based on gelatin methacryloyl (GelMA)/chitosan microspheres as a modular bioink for enhancing 3D neurite outgrowth and elongation, J. Colloid Interface Sci. 574 (2020) 162–173.

[55] P. Chen, C. Xia, S. Mei, J. Wang, Z. Shan, X. Lin, S. Fan, Intra-articular delivery of sinomenium encapsulated by chitosan microspheres and photo-crosslinked GelMA hydrogel ameliorates osteoarthritis by effectively regulating autophagy, Biomaterials 81 (2016) 1–13.

[56] N. Kamyar, R. Greenhalgh, T. Nascimento, E. Medeiros, P. Matthews, L. Nogueira, H. Haugen, D. Lewis, J. Blaker, Exploiting inherent instability of 2D black phosphorus for controlled phosphate release from blow-spun poly(lactide-co-glycolide) nanofibers, ACS Appl. Nano Mater. 1 (8) (2018) 4190–4197.

[57] J. Bai, Y. Zhang, Q. Fan, J. Xu, H. Shan, X. Gao, Q. Ma, L. Sheng, X. Zheng, W. Cheng, D. Li, M. Zhang, Y. Hao, L. Feng, Q. Chen, X. Zhou, C. Wang, Reactive oxygen species-scavenging scaffold with rapamycin for treatment of intervertebral disk degeneration, Adv Healthc Mater 9 (3) (2020), e1901186.

[58] Y. Bi, W. Duan, J. Chen, T. You, S. Li, W. Jiang, M. Li, G. Wang, X. Pan, J. Wu, D. Liu, J. Li, Y. Wang, Neutrophil decoys with anti-inflammatory and anti-oxidative properties reduce secondary spinal cord injury and improve neurological functional recovery, Adv. Funct. Mater. 31 (34) (2021).

[59] Q. Song, L. Liu, J. Yu, J. Zhang, M. Xu, L. Sun, H. Luo, Z. Feng, G. Meng, Dihydromyricetin attenuated Ang II induced cardiac fibroblasts proliferation related to inhibitory of oxidative stress, Eur. J. Pharmacol. 807 (2017) 159–167.

[60] A. Perelman, C. Wachtel, M. Cohen, S. Haupt, H. Shapiro, A. Tzur, JC-1, Alternative excitation wavelengths facilitate mitochondrial membrane potential cytometry, Cell Death Dis. 3 (2012) e430.

[61] K. Vincent, S. Mohanty, R. Pinelli, R. Bonavita, P. Pricop, T. Albert, C. Dahia, Aging of mouse intervertebral disc and association with back pain, Bone 123 (2019) 246–259.